J. Fluid Mech. (2021), *vol*. 918, A24, doi:10.1017/jfm.2021.311

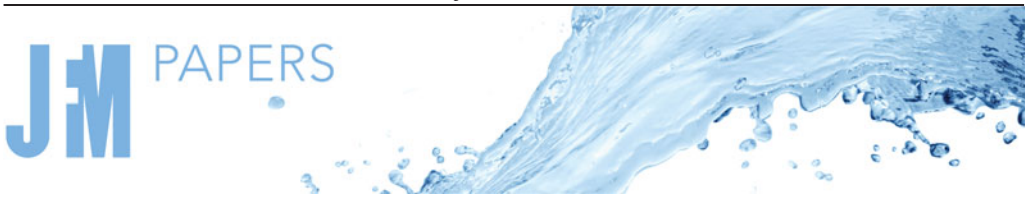

Flat plate drag reduction using plasma-generated streamwise vortices

X.Q. Cheng[1], C.W. Wong[1,†], F. Hussain[2], W. Schröder[3] and Y. Zhou[1,†]

[1]Center for Turbulence Control, Harbin Institute of Technology, Shenzhen 518055, China

[2]Department of Mechanical Engineering, Texas Tech University, Lubbock, TX 79409, USA

[3]Institute of Aerodynamics, RWTH Aachen University, 52062 Aachen, Germany

(Received 17 June 2020; revised 8 February 2021; accepted 4 April 2021)

We present an experimental study of a turbulent boundary layer (TBL) control on a flat plate using plasma actuators. Three different configurations of the actuators produce spanwise arrays of large-scale streamwise vortices (LSSVs). An ultra-high-resolution floating element (FE) force balance, developed in house and calibrated using μ-particle tracking velocimetry, is employed to measure wall friction. The FE captures a drag reduction (DR) of up to 26 % on the FE area (667×1333 wall units), downstream of the actuators. The local DR persists downstream, well after the LSSVs disappear. Both plasma-generated flow and the TBL under control are compared with an uncontrolled TBL. The maximum DR takes place when the LSSVs producing wall jets reach a spanwise velocity of 3.9 in wall units. The flow is altered by up to 29 % of the TBL thickness, with a drop in the new vortices due to the control-induced stabilization of the wall streaks. The local friction is characterized by three distinct spatial regions of drag increase, pronounced DR and drag recovery – all connected to the LSSVs. The LSSVs push the streaks to the middle between two adjacent actuators, suppressing transient growth and near-wall turbulent production. A DR mechanism is proposed.

Key words: boundary layer control, drag reduction, turbulent boundary layers

1. Introduction

Research on skin-friction drag reduction (DR) in the turbulent boundary layer (TBL) has attracted a great deal of attention because of its potential benefits in various engineering applications. Skin-friction drag is closely associated with quasi-streamwise vortices (QSVs), which occur mostly in the buffer layer, immediately above the large wall shear stress (WSS) sublayer (Kravchenko, Choi & Moin 1993; Orlandi & Jiménez 1994). The dynamics of QSVs in the near-wall region (Bernard, Thomas & Handler 1993) directly

† Email addresses for correspondence: cwwong@hit.edu.cn, yuzhou@hit.edu.cn

accounts for the generation of Reynolds shear stress and subsequently viscous drag. The well-known events, i.e. sweeps and ejections, streak-like structures, are all connected to QSVs (e.g. Kim 1983; Hussain 1986). Low-speed streaks (Kline *et al.* 1967) are a result of the ejection process induced by QSVs on their upwash side. Inflectional instability may occur in the lifted flows, resulting in bursts which are the major source of turbulence production (Kline *et al.* 1967). On the other hand, sweeps on the downwash side of QSVs induce wall-ward motion, adding large skin friction (Jeong *et al.* 1997).

Passive techniques, involving no energy input, have been investigated extensively for DR in the TBL, such as riblets, compliant and superhydrophobic surfaces, etc. The maximum DR associated with riblets or compliant surfaces is rather limited, in general to no more than 8 % (e.g. Walsh 1983; Choi, Moin & Kim 1993; Choi *et al.* 1997; Fukagata *et al.* 2008). One common drawback of riblets and compliant surfaces is that they become less efficient in DR and even increase drag when flow conditions (e.g. Reynolds number) change. Nature-inspired superhydrophobic surfaces may lead to a DR of up to 80 % (e.g. Daniello, Waterhouse & Rothstein 2009; Rastegari & Akhavan 2015). However, the performance of superhydrophobic surfaces deteriorates easily in practical environments (Yao, Chen & Hussain 2018).

Active techniques requiring energy input have been widely investigated because of their effectiveness in manipulating the TBL and achieving significant DR. Frequently used active strategies are blowing, or suction or both. Steady blowing through a spanwise slot in turbulent wall-bounded flows (e.g. Park & Choi 1999; Kim, Kim & Sung 2003) can achieve a local DR of 20 %–75 % downstream of the blowing slot. Suction through a short porous wall strip at a very high suction rate may cause re-laminarization of a TBL, producing a DR of approximately 50 % at 40–60 wall units downstream of the slot (Antonia, Zhu & Sokolov 1995). Periodic blowing through a spanwise slot can achieve a DR of 45 % at 20 wall units downstream of the slot (Tardu 2001), but produces a drag increase of 200 % over 80–300 wall units downstream of the slot. Synthetic jets through a spanwise array of streamwise slots yield a DR of 7 % (Rathnasingham & Breuer 2003). Another strategy is wall motion. The in-plane wall oscillations can produce a DR of 40 %–45 % (Baron & Quadrio 1996; Choi 2002), while wall-normal oscillations can reduce the spatially averaged drag by 7 %–17 % (e.g. Carlson & Lumley 1996; Endo, Kasagi & Suzuki 2000; Kang & Choi 2000). Spanwise- and streamwise-travelling waves (Du, Symeonidis & Karniadakis 2002; Quadrio, Ricco & Viotti 2009; Hurst, Yang & Chung 2014) can achieve a DR up to 50 %. However, it is difficult to implement wall oscillation or travelling waves in a technological system.

Dielectric barrier discharge (DBD) plasma actuators have recently attracted a great deal of interest because of their advantages, e.g. a simple structure, no moving parts and a rapid response. Plasma actuators have been successfully used to control laminar and turbulent flow separation on streamlined and bluff bodies. See Moreau (2007) and Corke, Enloe & Wilkinson (2010) for recent reviews on plasma actuators for aerodynamic applications. Choi, Jukes & Whalley (2011) experimentally studied the spanwise oscillation and spanwise-travelling waves induced by arrays of longitudinally aligned DBD plasma actuators for TBL. They suggested that the manipulation could lead to a DR of 45 %, although the drag change was not measured in their investigation. Whalley & Choi (2014) attempted to modify the near-wall turbulence structures based on plasma-generated spanwise-travelling waves but no drag measurement was made. In Mahfoze & Laizet's (2017) direct numerical simulation (DNS) in a turbulent channel, the plasma-generated spanwise jets suppressed QSVs and hence the sweep/ejection events, resulting in a 33.5 % DR. Note that their plasma-actuator-induced body force was simulated using a simplified

phenomenological model without solving the species transport equations for the plasma dynamics.

From the practical point of view, the externally generated large-scale streamwise vortices (LSSVs) are very efficient in achieving DR. They work by altering streaks and thus producing DR over an extended spatial domain containing numerous QSVs. This idea was initially proposed and demonstrated by Schoppa & Hussain (1998), who numerically simulated the LSSVs in a turbulent channel and achieved a DR of approximately 20 % via stabilization of streaks (Schoppa & Hussain 2002). Iuso *et al.* (2002) experimentally demonstrated in a turbulent channel flow that an array of jet-induced LSSVs yielded a DR of 15 %. Further, the DR area extended over nearly 50 times the channel width, but the drag was found to increase after the flow recovery due to the increment of mass flow rate resulting from the jet-added flow mass.

Recent DNS results (e.g. Yao *et al*. 2018) indicate that the spanwise flow of LSSVs can play an important role in the DR. Canton *et al.* (2016*a*,*b*) introduced numerically a spanwise volume force for the generation of LSSVs in a turbulent channel and achieved a DR of 18 % at a friction Reynolds number Re_τ of 180. With increasing Re_τ, however, the DR disappeared. In contrast, Yao *et al.*'s (2017, 2018) DNS data asserted that Canton *et al.*'s results were due to a misinterpretation of the forcing in the Schoppa–Hussain mechanism and demonstrated that the DR could still be achieved as Re_τ increased from 180 to 550, although it was slightly less pronounced, as expected. In spite of all these achievements, there has been rare successful experimental demonstration of DR using plasma actuators. The only experiment, which achieved DR by DBD plasma actuators, was carried out by Corke & Thomas (2018) and Thomas *et al.* (2019) who used pulsed-direct current (DC) actuators. Their actuators produced unidirectional and opposed wall jets in a TBL at a momentum-thickness-based Reynolds number Re_θ ranging from 4538 to 18 500. A maximum DR of 70 % measured using a floating element force balance was reported. Furthermore, a positive net energy saving was achieved given a small energy input required for the unsteady forcing with a very short DC pulse width. However, the altered flow structures under plasma control and the DR mechanism were not studied in detail. The challenge to apply the plasma actuator in a TBL for DR is that the induced wall jet may be associated with a downwash flow directly above the actuator due to mass continuity (Jukes & Choi 2013), increasing the skin friction (obviously more accentuated in channel flows). As such, plasma actuators must be carefully designed to generate wall jets – not merely LSSVs – that can effectively reduce the skin-friction drag.

This work aims to develop a plasma-actuated wall-jet control technique for the skin-friction DR in a TBL. Schoppa & Hussain's (1998) DNS demonstrated that skin-friction drag in a turbulent channel flow may be reduced by 20 % using externally generated LSSVs. Inspired by this, a number of plasma actuators are explored to generate LSSVs for manipulating TBL with a view to reducing skin friction. Measurements are made in the TBL with and without control using hot-wire, particle image velocimetry (PIV) and flow visualization techniques, and the data give insight into the physical mechanisms behind the drag variation. Experimental details are given in § 2. Results are presented and discussed in §§ 3 and 4. The work is concluded in § 5.

2. Experimental details

2.1. *Generation of fully developed TBL*

Experiments are performed in a closed-circuit wind tunnel at the Harbin Institute of Technology Shenzhen in China. The test section of the wind tunnel is 5.6 m long with

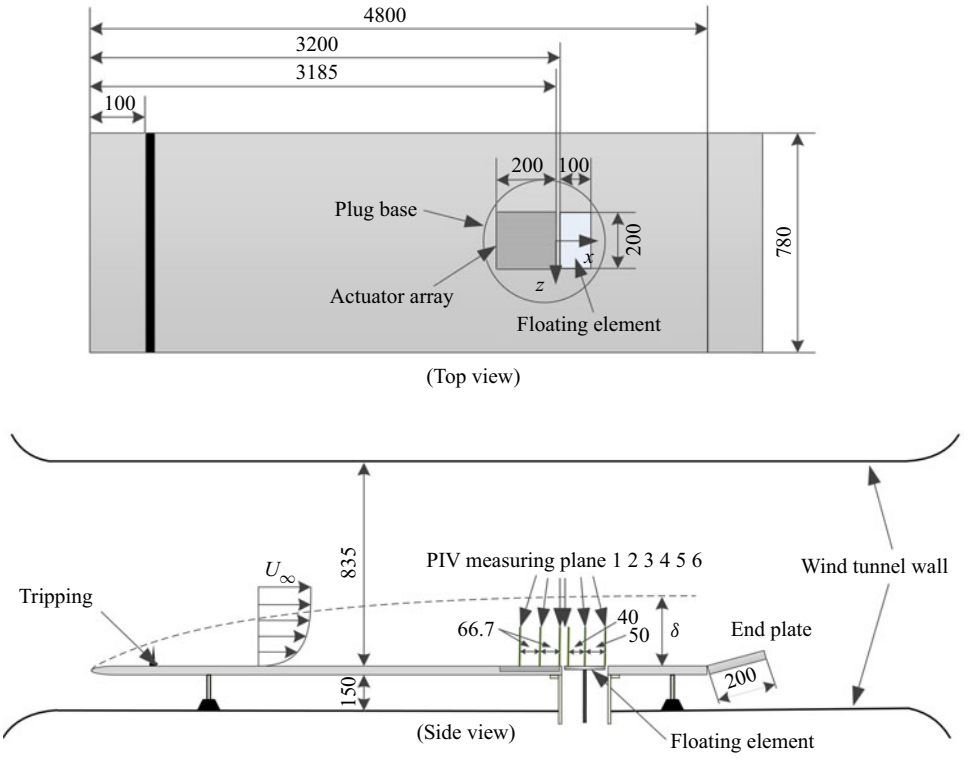

Figure 1. Schematic of the experimental set-up for the generation of a TBL (not to scale; dimensions in millimetres).

a cross-section of 0.8 m × 1.0 m. The flow in the tunnel is generated through an axial fan driven by an electric motor, with a maximum power of 75 kW. The free-stream velocity U_∞ in the test section can be varied between 1.5 and 50 m s^{-1}, with a longitudinal turbulence intensity of less than 0.4 % at $U_\infty = 2.4$ m s^{-1} where most of experiments are performed. A smooth Perspex flat plate of 4.8 m length, 0.78 m width and 0.015 m thick, with its leading edge rounded into an elliptic profile, is mounted in the test section (figure 1). Two spanwise-aligned arrays of M4 screws, separated longitudinally by 0.015 m and placed at 0.1 m downstream of the leading edge, trip the boundary layer. A 0.2 m long end plate, inclined by 12 °, is attached to the trailing edge of the plate to avoid flow separation from the leading edge (Qiao, Zhou & Wu 2017). The streamwise pressure gradient is carefully adjusted through slightly inclining the flat plate to 0.005 Pa m^{-1}. Most measurements are performed at 3.2 m downstream of the leading edge. The major parameters of the TBL are given in table 1, including the TBL thickness δ, momentum thickness θ, shape factor H_{12}, friction velocity u_τ ($\equiv\sqrt{\overline{\tau_w}/\rho}$, where τ_w is the local WSS, ρ is the density of air and the overbar denotes time averaging), viscous length scale $\delta_\nu = \nu/u_\tau$ (ν is the kinetic viscosity of air), time scale $t_\nu = \delta_\nu/u_\tau$, Re_θ and Re_τ based on θ and u_τ, respectively. Unless otherwise stated, the superscripts '+' and '*' in this paper denote normalization by the inner scales and outer scales in the absence of control, respectively. The coordinate system (x, y, z) is defined in figure 1, with the origin at the mid-point of the trailing edge of the actuators. The instantaneous velocities along the x, y and z directions are denoted by $U = \bar{U} + u$, $V = \bar{V} + v$ and $W = \bar{W} + w$, respectively, where u, v and w are the fluctuating components.

U_∞ (m s^{-1})	δ (mm)	θ (mm)	H_{12}	Re_θ	Re_τ	u_τ (m s^{-1})	δ_ν (mm)	t_ν (s)
2.4	85	9.2	1.41	1450	572	0.105	0.15	0.0014

Table 1. Characteristic parameters of the uncontrolled TBL.

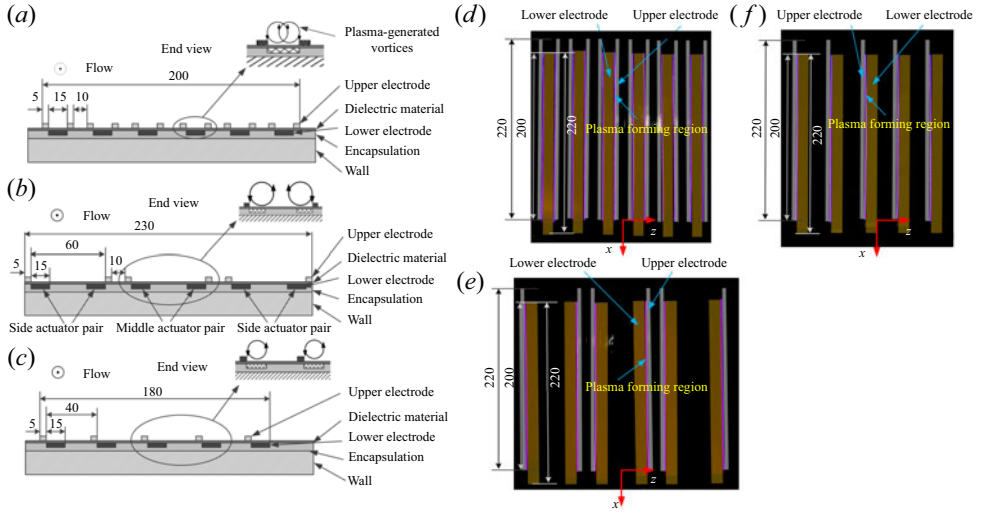

Figure 2. Schematic of three DBD plasma-actuator configurations (not to scale; dimensions in millimetres) and the photographs of the actuators and their discharges. (*a*,*d*) Configuration A, (*b*,*e*) configuration B, (*c*,*f*) configuration C. Control parameters of plasma actuators in (*d–f*): $E = 5.75$ kV$_{p\text{–}p}$, $f = 11$ kHz.

2.2. *Plasma actuators*

In the present experiments, the plasma-generated near-wall spanwise flow may interact with oncoming flow to form streamwise vortices (Jukes & Choi 2012, 2013), aiming to merge the streaks and suppress the streak instability. Three plasma-actuator configurations (i.e. A, B and C) are investigated, each with different lateral spacings between the upper electrodes of the actuators, number of electrodes and plasma discharge direction along the z-axis (figure 2). Configurations A and B generate counter-rotating LSSVs, with distinct downstream developments, such as the strength and separation between the LSSVs. On the other hand, configuration C generates co-rotating LSSVs.

The schematic of each plasma actuator is shown in figure 2. Each DBD plasma actuator consists of upper and lower electrodes separated by a dielectric panel made up of one layer of Mylar tape and one layer of Kapton tape, giving an overall thickness of approximately 0.23 mm ($\approx 1.5\delta_\nu$). The lower electrode is connected to the ground. The influence of the actuators on the flow is examined via a comparison between the hot-wire-measured mean and root-mean-square (r.m.s.) velocity profiles with and without the actuators on the wall. In the presence of actuators on the wall, the mean and r.m.s. velocity profiles deviate from their counterparts without actuators by less than 1.0 %. This deviation is ascribed to the uncertainty (1.0 %) of the hot-wire measurements. A near-wall flow is generated from the upper to the lower electrode using a sinusoidal alternating current (AC) waveform applied with a voltage $E = 3.50$–6.75 kV$_{p\text{–}p}$ (subscript p-p denotes peak-to-peak). Following Wang *et al.* (2017) and Wong *et al.* (2020), the frequency of E is fixed at 11 kHz, which is the

optimum operating frequency of the power supply. The plasma discharge occurs at the long edge of the upper electrode and extends to the lower electrode in the z-direction depending on the magnitude of E. Figure 2(d–f) shows an example of discharge for the three configurations at $E = 5.75$ kV$_{p\text{–}p}$. The plasma discharge is captured with a digital camera placed in the wall-normal direction. The upper and lower electrodes are marked as grey and yellow rectangles, respectively. The total streamwise length of the actuator array is 240 mm ($1600\delta_\nu$), and its effective length (excluding a length of 20 mm or $133\delta_\nu$ at each end for wire connection) is 200 mm ($1333\delta_\nu$). The discharge, shown in purple colour, has a streamwise length of 200 mm ($1333\delta_\nu$).

For configuration A, each actuator consists of two upper and one lower electrodes (figure 2a). The separation between the two upper electrodes of an actuator is 100 wall units, the same as the mean spanwise separation between streaks. As such, six actuators cover the spanwise extent of the FE. The lower electrode in each actuator is positioned between two upper electrodes, thus generating plasma discharge in opposite directions. These actuators produce adjacent counter-rotating LSSVs, seen in the PIV data. Configuration B includes six actuators, each consisting of one upper and one lower electrode. The total number of the upper electrodes or the 'total' discharge length is halved compared with configuration A. The separation between the upper electrodes of two adjacent actuators or one pair of actuators, as illustrated in figure 2(b), is 60 mm or 400 wall units. The corresponding lower electrodes are positioned such that the two actuators generate plasma discharges in opposite directions, resulting in non-colliding counter-rotating LSSVs. Five actuators (figure 2c) are used in configuration C, and each consists of one upper and one lower electrode, producing plasma discharge in the same direction along the z-axis. The separation between the upper electrodes of two adjacent actuators is 267 wall units. Configuration C generates co-rotating LSSVs.

The total power consumption is estimated from voltage E and current I for each configuration. The value of I is measured across a non-inductive resistor (100 Ω) connected in series between the lower electrode and the earth.

2.3. *Hot-wire measurement*

A single, constant temperature hot-wire of 5 μm ($0.033\delta_\nu$) in diameter and approximately 1.25 mm ($8.3\delta_\nu$) in length is mounted on a computer-controlled traversing system to measure the streamwise velocity across the TBL. The spatial resolution of the traversing system is 3.125 μm ($0.021\delta_\nu$) in the wall-normal direction. A total of 13 measurement points, with an increment of 50 μm ($0.33\delta_\nu$), are taken in the near-wall region to estimate the velocity gradient in the viscous sublayer. The longitudinal distance between the hot-wire and the trailing edge of the plasma actuators is 25 mm ($167\delta_\nu$) or more, well exceeding the critical separation (15 mm) suggested by Choi *et al.* (2011), to avoid destructive arcing (Choi *et al.* 2011). Tests have been conducted to measure the hot-wire signals at $x = 25$ mm in the absence of incident flow, with and without plasma discharge. There is no appreciable difference in $\bar{U}$ observed between the two cases, suggesting a negligible effect of the plasma discharge on the hot-wire measurements. As the high-voltage power supply (CTP-2000 K) for generating the plasma produces an electronic noise of around 1.10 kHz, the sampling rate for the acquisition of the hot-wire data is chosen to be 3 kHz, with a cutoff frequency of 1 kHz. The sampling duration for each point is 40 s (28000 t_ν), adequately long for the convergence, to within 1 % uncertainty, of the mean and r.m.s. values of the velocity. The hot-wire is calibrated with a Pitot tube connected to a micro-manometer (FCO510, with an accuracy of 0.25 % of the pressure reading and 0.001 Pa resolution). The same Pitot tube and the

micro-manometer are used to measure the streamwise pressure gradient along the flat plate, as well as the pressure difference between the upper and lower sides of the floating element (FE) in the force balance measurements. Following Hutchins & Choi (2002), the first wall-normal position y_0 of the hot-wire probe is obtained from linear fitting to $\bar{U}$ in the viscous sublayer. The fitting curve in the linear region can be written in the form of $\bar{U} = ay_{ref} + b$, where a and b are constants determined from fitting the equation to the measured data points, and y_{ref} is the wall-normal position away from the first hot-wire measurement point. Letting $\bar{U} = 0$ yields $y_{ref} = -b/a$ or $y_0 = b/a$.

2.4. *PIV and smoke-wire flow visualization*

A LaVision time-resolved PIV system is used to measure the flow structure, generated by plasma actuators, and the manipulated TBL in three orthogonal planes, i.e. the y–z, x–z and x–y planes. The flow is seeded with fog, with an average particle size of 1 μm, generated from peanut oil by a TSI 9307-6 particle generator. The flow is illuminated by 1.2 mm ($8\delta_v$) thick laser sheets shining through the side window, produced by a dual beam laser system (Litron LDY304-PIV, Nd: YLF, with a maximum energy output of 30 mJ per pulse) in conjunction with spherical and cylindrical lenses. For measurements in the y–z planes, one high-quality mirror of 80 mm × 150 mm is fixed on the plate at $x = 0.51$ m, 45 ° with respect to the y–z plane, downstream of the plasma actuator so that the images in the plane could be captured by a high-speed camera (Imager pro HS4M, 4-megapixel sensors, 2016 × 2016 pixels resolution) placed outside the working section. The image covers an area of 108 × 108 mm. For measurements in the x–z plane, the laser sheet shines through the plane of $y^+ = 24$. For measurements in the x–y planes, the laser sheet shines through the planes of $z^+ = 0$, 133 and 183. The image is captured by the same camera with a sampling frequency of 200 Hz. The total number of images captured is 1500 pairs for measurements in the y–z or x–z plane with a sampling frequency of 300 Hz. This number is increased to 2700 for measurements in the x–y plane to ensure the convergence of the dissipation and production of turbulent kinetic energy (TKE) to less than 1.5 %. In the image processing, the spatial cross-correlation, with an interrogation window of 32 × 32 pixels and a 50 % overlap along both directions of the image, determines the velocity vectors – a total of 15 876. The same number of vorticity data is obtained. The resulting spatial resolution is 0.9, 1.6 and 0.5 mm, or 6.0, 10.7, and 3.3 wall units for the y–z, x–z and x–y planes, respectively. The same PIV system is used for smoke-wire flow visualization experiments conducted in two x–z planes at $y^+ = 20$ and 50 with and without control. The value of U_∞ is set at 1.8 m s^{-1} in order to ensure high quality flow visualization images. The smoke-wire is placed at $y^+ = 17$ or 47, and 150 mm (1000 wall units) downstream of the leading edge of the plasma actuators, parallel to the wall and normal to the free stream. The flow images are captured at 200 frames per second.

2.5. *The μ-particle tracking velocimetry measurement*

A μ-particle tracking velocimetry (μ-PTV) technique is deployed to measure the streamwise velocity near the wall, hence to measure the local WSS at $U_\infty = 2.4$–5.0 m s^{-1}, which will be used to calibrate the FE balance. The same camera as used in the PIV measurements is fitted with a long-distance microscope lens (Model K2) and two zoom lenses with a magnification factor of 2 so that the field of view is as small as 6.1 mm × 6.1 mm in the x–y plane (figure 4). As such, the spatial resolution reaches as high as 330 pixels mm^{-1} – adequate for our need. Due to a large loss of the light intensity through the long-distance microscope lens, the μ-PTV measurement requires a much more

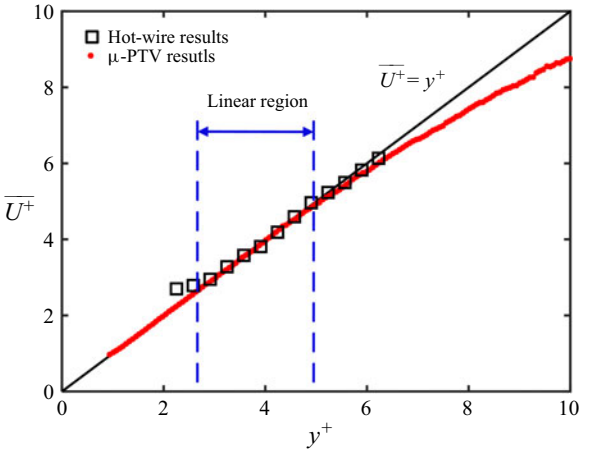

Figure 3. Comparison of the hot-wire- and μ-PTV-measured time-averaged streamwise velocities $\overline{U^+}$.

powerful laser than the PIV measurement. A low-frequency laser source (Vlite-200), with a power of 200 mJ per pulse, is used to illuminate the flow field. The flow is seeded with particles of Di-Ethyl-Hexyl-Sebacat, with an average diameter of 1 μm, generated by a commercial particle generator (TSI 9307-6). The time interval between the two frames of an image pair is 40–75 μs (0.053–0.091 t_v), depending on U_∞. A total of 10 000 image pairs are captured, sampled at 15 Hz for each U_∞. The μ-PTV data are processed by an in-house developed algorithm. More details on this algorithm are given by Li *et al.* (2015, 2017). A spatial bypass filter is used to subtract the background of the images so that the centroid of each particle can be identified and tracked. As a result, the displacement of each particle and hence its velocity is easily computed. The captured flow field is divided into small strips parallel to the wall, with a height of 10 μm or 0.067–0.127 wall units depending on U_∞. The velocity vectors averaged within a strip to give the mean velocity. The local time-averaged WSS can then be calculated from the mean velocity gradient in the wall-normal direction in the viscous sublayer. Following Benedict & Gould (1996) and Li *et al.* (2017), the variance of the mean streamwise velocity $\bar{U}$ may be written as $\mathrm{var}(\bar{U}) = \overline{u^2}/N$, where N is the number of samples. Then, the theoretical sampling error of $\bar{U}$ with a 95 % confidence interval is given by $\Delta U = 1.96\sqrt{\mathrm{var}(\bar{U})}$. This error is less than 0.8 % at $U_\infty = 2.4$–$5\ \mathrm{m\ s^{-1}}$ for the present μ-PTV measurements. Figure 3 presents the distributions of the mean streamwise velocity near the wall measured using both μ-PTV and hot-wire at $U_\infty = 2.4\ \mathrm{m\ s^{-1}}$ where the DR measurements are conducted. The inner-scale normalized streamwise velocity follows $\overline{U^+} = y^+$ at $2.5 < y^+ < 5$, by both μ-PTV and hot-wire measurements. The departure of the hot-wire-measured WSS is less than 2 % of the μ-PTV data. This comparison provides a validation for the hot-wire measurements.

2.6. *Direct skin-friction measurement*

It is a challenge to measure directly the skin-friction drag of a low Re_θ TBL, especially to resolve the variation of this force under control. The drag on the FE is presently of the order of 10^{-4} N, which is much smaller than that (10^{-2}–10^{-1} N) in Corke & Thomas (2018) and Thomas *et al.* (2019). A FE balance, schematically shown in figure 4, was built in house to measure this drag on a FE of area $A = 0.1 \times 0.2\ \mathrm{m^2}$ whose leading edge is 15 mm (100 wall units) downstream of the trailing edge of the actuators (figure 1). The balance comprises

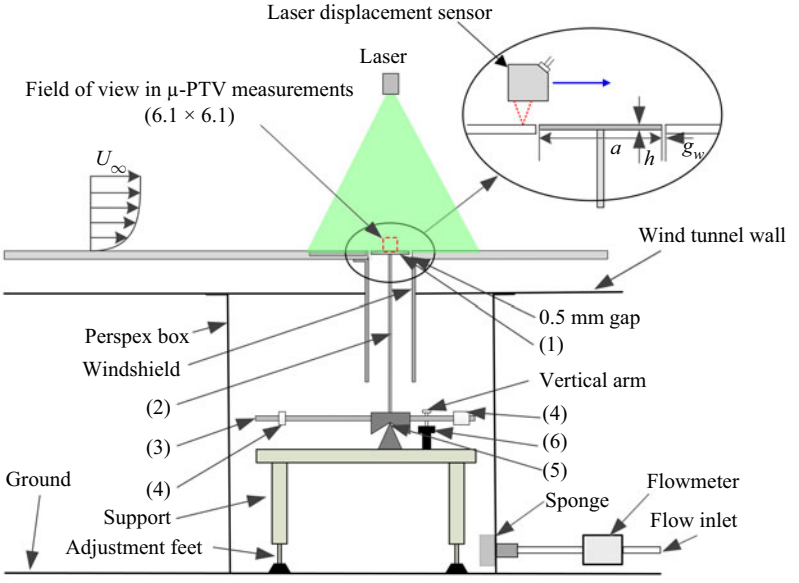

Figure 4. Schematic of the FE balance and μ-PTV arrangement (not to scale; dimensions in mm). (1) Rectangular FE, (2) vertical beam, (3) horizontal steel rod, (4) counter-weight, (5) knife edge, (6) load cell.

of 6 main parts: (1) a rectangular FE of 0.2 m in spanwise width and 0.1 m in longitudinal length, (2) a vertical beam of length × width × thickness = 0.41 × 0.07 × 0.006 m, (3) a horizontal steel rod of 0.465 m in length and 0.012 m in diameter, (4) two counter-weights (12.5 and 25 g installed at the front and rear ends of the rod, respectively), (5) a knife edge, and (6) a force load cell (Honeywell M34, range ±50 g). The FE (1) is mounted on the vertical beam (2) which sits on the knife edge (5).

The FE balance follows the concept of Krogstad & Efros (2010), who managed to measure the WSS of the order of 10^{-1} N in a rough-wall TBL. However, the present WSS on a smooth wall is much smaller, of the order of 10^{-4} N. As such, a series of improvements have been made to improve the resolution and minimize the measurement errors. Firstly, the balance works on the lever principle, and the horizontal drag force on the FE is amplified 45 times (nine times larger than that in Krogstad & Efros 2010). The force amplification depends on the length of the vertical beam and the separation between the knife edge and the load cell. The vertical beam is made of aluminium alloy for high stiffness (90 N mm^{-2}) with light weight (230 g). A relatively heavy and long horizontal steel rod (3) is used to damp out any FE vibration. The movement of the upper end of the beam is less than 1.5 μm, at $U_\infty = 0$–5.0 m s^{-1}; that is, the FE effectively does not rotate. Secondly, the amplified force pivoted about the knife edge is measured using a load cell, rather than a commercial weighing scale as used by Krogstad & Efros (2010), installed at 9 mm away from the knife-edged support perpendicular to the horizontal axis. The two counter-weights (4) act to preload the load cell to ensure its operation in the linear range. The load cell provides a more stable signal and captures the normal force only, with a resolution of 7.5×10^{-4} N. Amplified 45 times, the skin friction captured by the balance can be as small as 1.7×10^{-5} N. The force signal is offset, amplified and sampled at 1 kHz for the duration of 30 s using an National Instruments (NI) data acquisition system. Thirdly, as the flow outside the wind tunnel under the FE can greatly influence the force measurements (Baars *et al.* 2016), the FE balance is housed in a

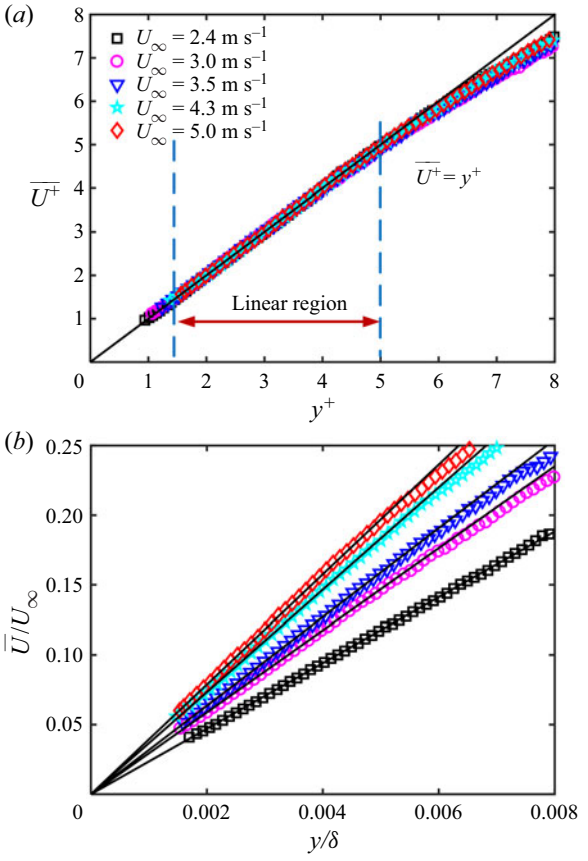

Figure 5. Wall-normal distributions of μ-PTV-measured mean streamwise velocity in the near-wall region normalized by (*a*) inner scales and (*b*) outer scales.

sealed transparent Perspex box. The box is pressurized to that within the test section. Fourthly, the gap between the FE and the flat plate is only 0.5 mm. The FE-to-plate misalignment is measured using a high-resolution laser displacement sensor (OPTEX CD33) with a resolution of 7.5 μm. As shown in the inset of figure 4, this sensor, mounted on a three-dimensional traversing system with a spatial resolution of 3.125 μm, moves horizontally from the surrounding plate to the FE. The misalignment, determined from the distance between the two wall surfaces, is kept less than 7.5 μm by carefully adjusting the height of the adjustable feet (figure 4). Therefore, the gap-induced error is less than 1 % (Allen 1977). Finally, the experimental set-up is carefully adjusted to ensure a streamwise pressure gradient of less than 0.005 Pa/m, and the FE is chosen to be 1 mm in thickness to minimize the difference between the static pressures on its leading and trailing edges. As a result, the error from the pressure gradient is reduced to less than 0.04 %. With these measures implemented, the balance is found to be able to capture reliably a skin-friction force of the order of 10^{-4} N.

The calibration of the present balance is another challenge. The conventional pulley system could not be used since the friction force between the wire and pulley is of the same order as the skin-friction drag. A novel and reliable calibration method is proposed. It has been confirmed that the μ-PTV-measured u_τ varies less than 1 % from the leading edge of the FE to the trailing edge. Furthermore, the flow is statistically two-dimensional

in the absence of control. As such, the measured u_τ at the centre of the FE is taken as the mean value over the FE. This prompts us to determine the skin-friction force F on the FE over $U_\infty = 0$–$5\ \mathrm{m\ s^{-1}}$, which provides a calibration for the output voltage E_{output}. As shown in figure 5, the μ-PTV-measured mean streamwise velocity follows a linear variation near the wall, with an appreciable departure from the linearity only for $y^+ > 5$ for the U_∞ range examined. The local $\overline{\tau_w}$ is calculated from the velocity gradient in the viscous sublayer through

$$\overline{\tau_w} = \mu \frac{\mathrm{d}\bar{U}}{\mathrm{d}y} \quad \text{for } y^+ \leq 5, \tag{2.1}$$

where $\mu\ (= \rho\nu)$ is the dynamic viscosity of air. The uncertainty of $\overline{\tau_w}$ is analysed following Hutchins & Choi (2002). We calculate $\mathrm{d}\bar{U}/\mathrm{d}y$ by

$$\mathrm{d}\bar{U}/\mathrm{d}y = \frac{\sum_{i=1}^{n} (y_i - \langle y \rangle_n)(\overline{U_i} - \langle \bar{U} \rangle_n)}{\sum_{i=1}^{n} (y_i - \langle y \rangle_n)^2}, \tag{2.2}$$

where n is the number of points used to calculate $\mathrm{d}\bar{U}/\mathrm{d}y$, ranging from 15 to 32 depending on U_∞, and $\langle\ \rangle_n$ represents the average over n points. Then the standard error of $\overline{\tau_w}$, due to the least-squares fitting and velocity measurement uncertainty, is

$$\mathrm{S.E.}(\overline{\tau_w}) = \frac{\mu\sigma_u}{\left[\sum_{i=1}^{n} (y_i - \bar{y})^2\right]^{1/2}}, \tag{2.3}$$

$$\sigma_u^2 = \frac{\sum_{i=1}^{n} (\overline{U_i} - \langle \bar{U} \rangle_n)^2 - (\mathrm{d}\bar{U}/\mathrm{d}y) \sum_{i=1}^{n} (y_i - \bar{y})(\overline{U_i} - \langle \bar{U} \rangle_n)}{n - 2}. \tag{2.4}$$

The uncertainty of $\overline{\tau_w}$ or $\mathrm{S.E.}(\overline{\tau_w})/\overline{\tau_w}$ is below 0.6 % over the range of U_∞ examined (figure 5). Then the skin-friction drag force F is approximated as

$$F = \overline{\tau_w} A = \rho u_\tau^2 A. \tag{2.5}$$

As shown in figure 6, E_{output} and F are linearly related. The maximum deviation between the data points and the fitting curve is 1.2 % for the entire calibration range.

The skin-friction coefficient c_f, defined as

$$c_f = \frac{F/A}{0.5\rho U_\infty^2}, \tag{2.6}$$

is presented in figure 7. The deviation of the present data from the Coles–Fernholz relation ($c_f = 2/[1/0.384 \times \ln(Re_\theta) + 4.127]^{-2}$) (Nagib, Chauhan & Monkewitz 2007) is less than 3.5 %, which provides us with additional confidence in the present FE-force balance.

3. Control performance

3.1. *TBL in the absence of control*

It is important to ensure the generation of a fully developed TBL at the leading edge of the plasma actuators. The Reynolds number based on the streamwise distance Re_x

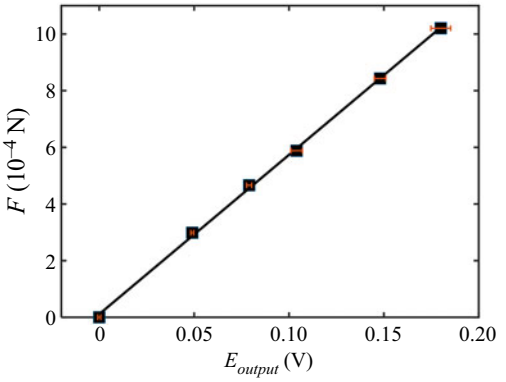

Figure 6. Calibration curve of the FE-force balance, where $F = \rho u_\tau^2 A$ (u_τ is determined from the μ-PTV-measured streamwise velocity gradient measured at the centre of the FE) and E_{output} are the skin-friction drag on the FE and the output voltage of the balance, respectively. The error bars in red colour denote the standard deviation of the output voltage for 6-time repeated measurements.

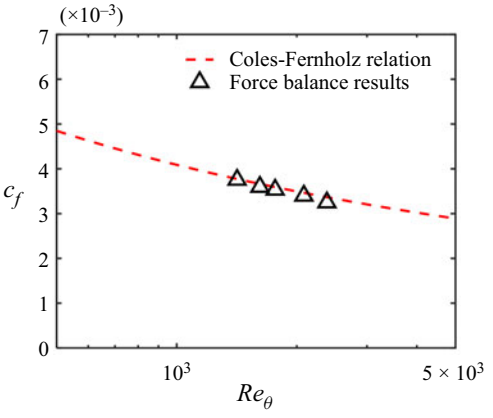

Figure 7. Comparison of the skin-friction coefficient c_f measured using the force balance with the Coles–Fernholz relation.

($= U_\infty x/\nu$) between the leading edges of the flat plate and plasma actuators is 4.6×10^5 without tripping. Once tripped, the distribution of the mean streamwise velocity $\overline{U^+}$ (figure 8*a*) across the boundary layer measured at the leading edge ($x^+ = -1333$, $z^+ = 0$) and also downstream of the actuators ($x^+ = 167$, $z^+ = 0$) collapses well with the law of wall (Pope 2001). The r.m.s. value u^+_{rms} of the fluctuating streamwise velocity agrees well with Schlatter *et al.*'s (2009) DNS and De Graaff & Eaton's (2000) experiments. The results indicate that the TBL is indeed fully developed at these locations.

3.2. *Plasma-induced flow structure*

For configuration A, one pair of counter-rotating LSSVs is generated downstream of each actuator, as is evident in the PIV images (figure 9*a*) captured at the trailing edge of the actuators, i.e. $x^+ = 0$, covering $-300 \leq z^+ \leq 300$. At $E = 5.75$ $\mathrm{kV_{p\text{–}p}}$, the LSSVs collide with each other, forming strong upwash between the vortices generated by one actuator but downwash between adjacent actuators (figure 9*a*). The vortices within the

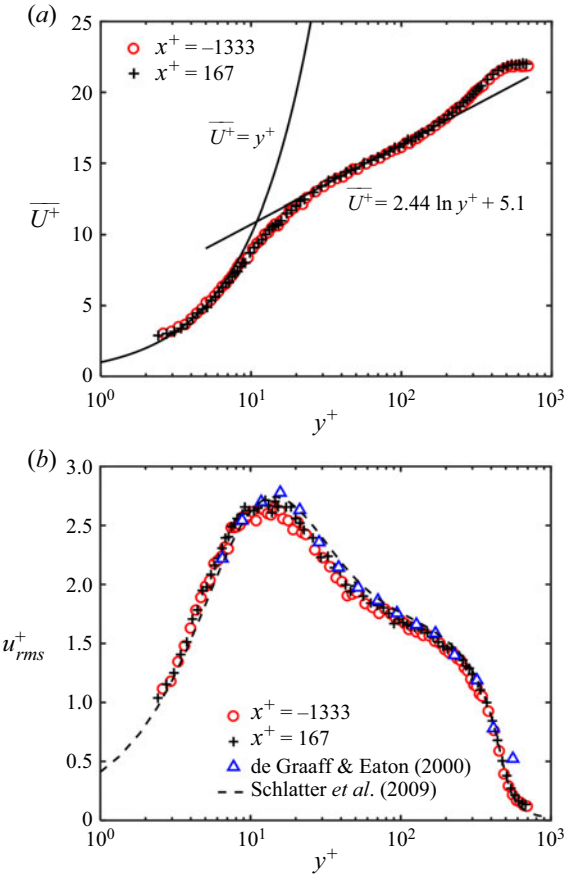

Figure 8. Profiles of (*a*) mean streamwise velocity $\overline{U^+}$ at the leading edge ($x^+ = -1333$, $z^+ = 0$) of actuators and the test location ($x^+ = 167$, $z^+ = 0$) and (*b*) r.m.s. value u^+_{rms} of the fluctuating component u.

same counter-rotating pair may be strengthened by their interactions (Lögdberg, Fransson & Alfredsson 2009) and progressively lifted away from the wall by mutual induction (Jukes & Choi 2012). Pauley & Eaton (1988) observed that counter-rotating streamwise vortices with common upflow lifted up while developing downstream. They proposed that the image vortices (Ersoy & Walker 1985) in the wall caused the counter-rotating streamwise vortices to move towards each other and then move away from the wall. There are two consequences of this collision. First, the pair, as they come closer, become a strong vortex dipole and move away from the wall via mutual induction. Second, when pressed against each other, the two vortices undergo simultaneous weakening downstream because of the continual planar reconnection via cross-diffusion (Hussain & Duraisamy 2011; Yao & Hussain 2020). Clearly, the actuators' effect will thus decrease with increasing length due to mutual induction of adjacent LSSVs, discouraging the use of very long actuators. The optimum actuator length will depend on the spanwise spacing of the actuators, on the driving voltage which controls the strength of the wall jet and also on the local friction Reynolds number. These details are beyond the scope of the current paper and must await careful future studies. Note that due to the large separation between the two upper electrodes in configuration B, the counter-rotating LSSVs do not come close enough to each other and are not significantly altered by cross-diffusion (figure 9*b*).

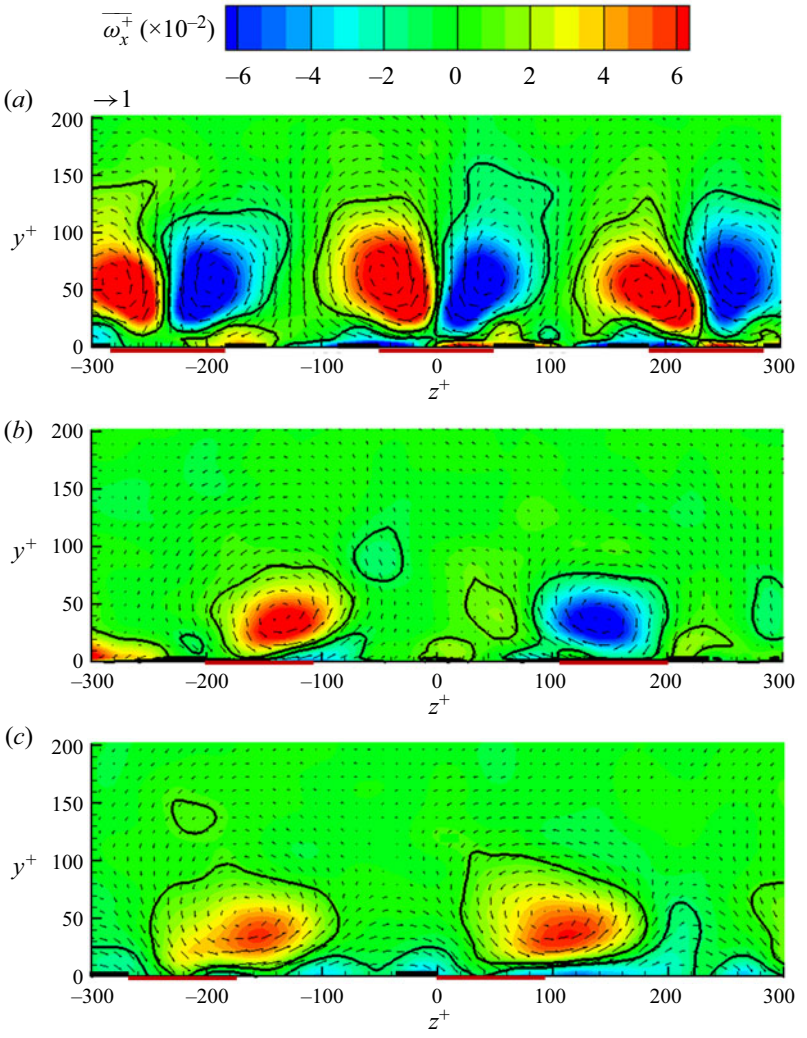

Figure 9. Time-averaged velocity vectors $(\overline{V^+}, \overline{W^+})$ and iso-contours of vorticity $\overline{\omega_x^+} = \overline{\mathrm{d}V^+/\mathrm{d}z^+} - \overline{\mathrm{d}W^+/\mathrm{d}y^+}$ in the y–z plane at the trailing edge ($x^+ = 0$) of the plasma actuators. Configurations (*a*) A, (*b*) B and (*c*) C. The bold black contour denotes the level of 10 % of the maximum vorticity. The positive and negative electrodes are shown in black and red colours, respectively. Control parameter: $E = 5.75\ \mathrm{kV_{p\text{–}p}}$.

Furthermore, these LSSVs occur closer to the wall than in configuration A – this is to be expected because the two LSSVs of each pair are too far apart to be able to significantly move each when away from the wall via mutual interaction, and they are weakened much less as vorticity cross-diffusion is much lower. The inner-scale normalized circulation Γ^+ of configuration B, calculated along the contour line of 10 % of the maximum vorticity, is 9.7, which is considerably smaller than that (15.8) for configuration A. This apparent contradiction can be reconciled by the fact that because the LSSVs remain closer to the wall in configuration B and thus undergo faster decay by higher viscous dissipation. Configuration C produces plasma discharge in the same direction along the z-axis, generating co-rotating LSSVs, as shown in figure 9(*c*). At $E = 5.75\ \mathrm{kV_{p\text{–}p}}$, the vortices are far away from the plasma discharge region of an actuator due to the

unidirectional plasma-induced wall jet (Corke *et al*. 2010), so that the LSSVs move along the same spanwise direction. The LSSVs are expected to decay slowly and to move laterally downstream (Jukes & Choi 2012) mainly by the mutual induction of the image vortices.

3.3. *Dependence of DR on actuator configuration*

Both FE-force balance and hot-wire are used to measure the DR downstream of the actuators, capturing the spatially averaged drag variation and the local drag variation along the spanwise and streamwise directions, respectively. The control performance is evaluated through the drag variation $\Delta F = (F_{on} - F_{off})/F_{off}$, where F_{off} and F_{on} are the skin friction on the FE without and with control, respectively. Note that the FE is mounted 15 mm downstream of the trailing edge of the actuators (figure 1). The ΔF depends on the E imposed as well as on the configuration, as shown in figure 10(*a*), where the error bars indicate the standard deviation of ΔF of six repeated measurements. Given the same E, the power consumption differs from each other between the configurations in figure 10(*a*) due to a difference in the number of electrodes and hence in the total 'effective' discharge length. In general, ΔF dips rapidly with increasing E for configurations A, B and C. Configuration B always corresponds to the smallest ΔF of all, and configuration A comes next in terms of the control performance. The LSSVs in configuration A may collide with each other as explained above, resulting in less DR than in B. Note that the larger separation between the LSSVs in B lengthens the wall jets, with corresponding weakening of their effectiveness (Yao *et al*. 2018). The maximum DR of both configurations A and B occurs at $E = 5.75\ \mathrm{kV_{p\text{–}p}}$, beyond which the drag recovers rapidly. The DR is connected to the plasma-generated vortices (figure 9). An increase in E increases the wall-jet velocity (Jukes *et al.* 2006) and also the vortex strength, and hence a more pronounced drop in skin friction (Yao *et al*. 2018). However, beyond a certain level of E, say, at $E > 5.75\ \mathrm{kV_{p\text{–}p}}$, the vortices grow rapidly, causing an increase in vortex-induced shear stress or drag in the TBL (Schoppa & Hussain 1998; Iuso *et al.* 2002). A similar observation was made previously. Yao *et al*. (2018) found from their DNS data that the skin-friction drag was reduced by the spanwise wall jet with the spanwise velocity low, but not high. They advocated that the spanwise wall jet suppresses the random turbulent shear stress associated with the QSVs in the TBL, while introducing additional coherent shear stress caused by the strong wall jets. With increasing E, the LSSVs are strengthened, shown later, and the coherent shear stress may exceed the reduction of the random shear stress, leading to a rise in drag. This is clear as with increasing wall-jet speed, the downwash also gets stronger, making the wall jet thinner and stronger and thus also increasing $(\mathrm{d}U/\mathrm{d}y)_w$ (the subscript 'w' denotes the value on the wall) and hence the WSS (Jeong *et al.* 1997).

The DR of configuration C is always less than that of A or B. The maximum DR is only 10 % for configuration C, but approximately 20 % and 26 % for A and B, respectively. Unlike the opposed spanwise wall jets of configurations A and B, configuration C generates co-rotating LSSVs and the upwash induced by one vortex counters the downwash of the adjacent vortex. The counteraction could be avoided if the vortex spacing exceeds three times the vortex height (Jukes & Choi 2012). The spanwise spacing of the co-rotating LSSVs generated by plasma configuration C is 267 wall units, less than 3 times the vortex height (110 wall units). As a matter of fact, the interaction between two adjacent vortices is evident in the PIV-measured time-averaged velocity field (figure 9*c*), where the upwash of the right vortex counters the downwash of the left vortex. As a result, the strength of the vortices is the smallest among the three configurations. Γ^+ in configuration C is only 7.9, which is appreciably smaller than in A and B. This interaction in the shear region may further lead to additional turbulence intensity

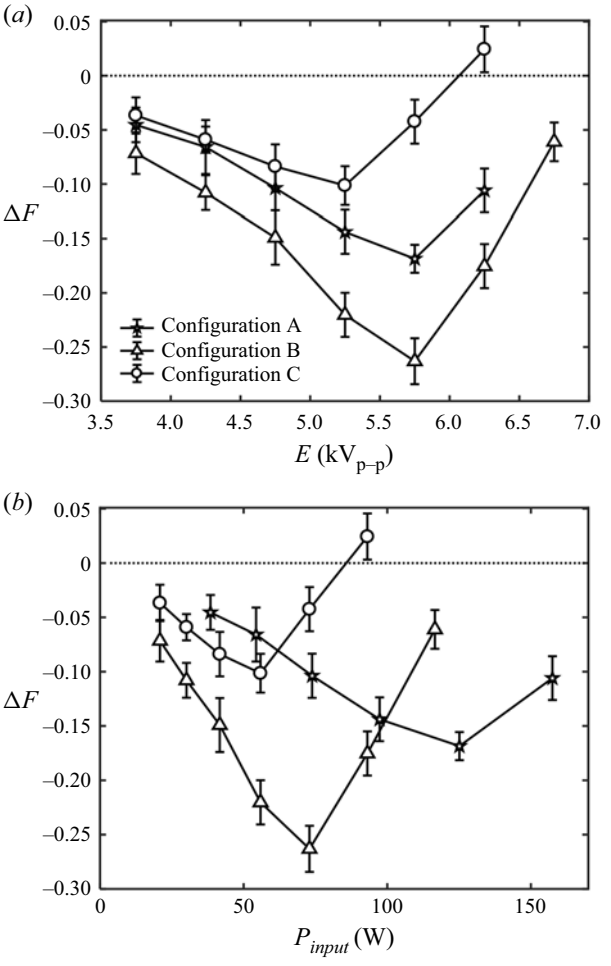

Figure 10. (*a*) DR $\Delta F = (F_{on} - F_{off})/F_{off}$ for configurations A, B and C, where F_{on} and F_{off} are the floating-element-balance-measured skin-friction drag with and without the plasma actuator operated, respectively. Here, E is the applied voltage. The error bars mark the standard deviation of the 6-time repeated results. (*b*) Variation of ΔF with the power input of three plasma-actuator configurations.

(Pauley & Eaton 1988). Consequently, the DR of configuration C is the smallest of the three. This is to be expected as the effective area of the intense wall jets is much less.

Figure 10(*b*) presents the relation between ΔF and the power consumption P_{input} where

$$P_{input} = \int_{t_1}^{t_2} E(t)I(t)\,\mathrm{d}t. \tag{3.1}$$

In (3.1), $E(t)$ and $I(t)$ are the instantaneous voltage and current signals, and t_1 and t_2 are the starting and ending times of sampling, respectively. As P_{input} is correlated with the applied voltage, the DR variation with P_{input} is similar to that with E. Obviously, configurations A and B reach their maximum DR at the same voltage ($E = 5.75$ kV$_{p-p}$). However, the power consumption of configuration A is much larger than that of B, as the total discharge length of the former is two times more than that of the latter.

Figure 11 presents the control efficiency $\eta = P_{saved}/P_{input}$, where $P_{saved} = (F_{off} - F_{on})$ U_∞ is the time-averaged power saving due to plasma control, and P_{input} is the total energy

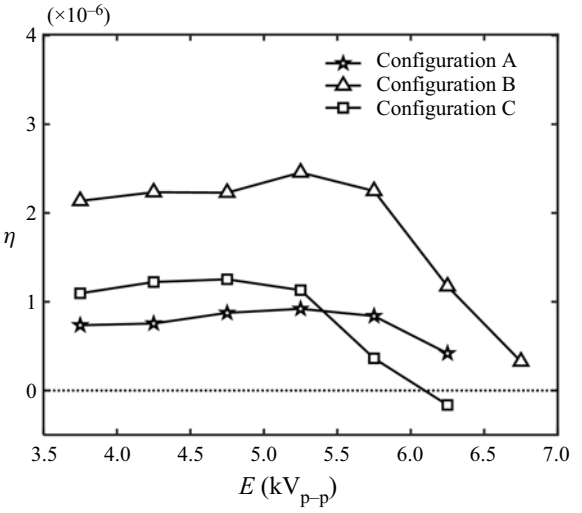

Figure 11. Control efficiency $\eta = (F_{off} - F_{on})U_\infty/P_{input}$ for configurations A, B and C. Here, P_{input} is the power consumption, F_{on} and F_{off} are skin-friction drag acting on the FE with and without control, respectively.

input to manipulate the TBL. The power saved is several orders of magnitude smaller than the power consumed. Note that P_{saved} is calculated from the variation in drag on the FE and the actual power saving over the entire drag-reduced area will be much larger. Among the three configurations, the maximum η is achieved at $E = 5.25$ kV$_{p-p}$ in B. The η of configuration B is in general largest of all (figure 11), outperforming other configurations in terms of the η as well as DR. As such, following discussion will focus on configuration B only.

3.4. *Dependence of plasma-generated streamwise vorticity on applied voltage*

For configuration B, the spatially averaged streamwise vorticity $\langle\overline{\omega_x}\rangle_v$ over the vortex enclosed by the contour of 10 % of the maximum vorticity is calculated from the PIV-measured time-averaged vorticity data in the y–z plane at the trailing edge ($x^+ = 0$) of the middle plasma-actuator pair. For $E < 4.25$ kV$_{p-p}$, $\langle\overline{\omega_x}\rangle_v$ scales linearly with $E^{3.5}$ (figure 12) – similar to Wicks, Thomas & Corke's (2015) finding. However, when $E > 4.25$ kV$_{p-p}$, the rise in $\langle\overline{\omega_x}\rangle_v$ with E is slowed down and $\langle\overline{\omega_x}\rangle_v \propto E^{1.6}$. This variation with E exceeding a certain level is not unexpected. Thomas *et al.* (2009) found that the plasma-generated body force was proportional to $E^{3.5}$ at low voltages but to $E^{2.3}$ at high voltages. With $\langle\overline{\omega_x}\rangle_v$ scaled with this body force (Wicks, Thomas & Corke 2015), $\langle\overline{\omega_x}\rangle_v$ is expected to increase with E faster at low voltages but slower at high voltages. The difference between our and Thomas *et al.*'s (2009) results may be due to a difference in the dielectric material or its thickness between the two studies. The dielectric panel is presently made of 0.073 mm thick Mylar tape and 0.055 mm thick Kapton tape but of a 6.35 mm thick Telfon sheet in Thomas *et al.* (2009).

3.5. *Relation between DR and maximum spanwise velocity*

It is of interest to investigate the dependence of ΔF on wall-jet velocity. The maximum spanwise velocity $|\overline{W_{max}}|^+$ in configuration B is calculated from the PIV-data in the y–z

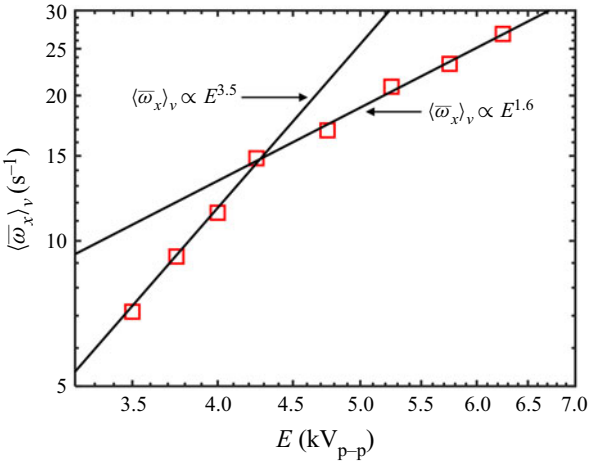

Figure 12. Spatial-averaged streamwise vorticity $\langle\overline{\omega_x}\rangle_v$ over the vortex enclosed by the contour of 10 % of the maximum vorticity. The value of $\langle\overline{\omega_x}\rangle_v$ is calculated from the PIV-measured time-averaged vorticity data in the y–z plane at the trailing edge ($x^+ = 0$) of the middle plasma-actuator pair. Here, E is the applied voltage (configuration B).

plane of $x^+ = 0$ (figure 13). The ΔF decreases with increasing $|\overline{W_{max}}|^+$ until reaching its minimum at $|\overline{W_{max}}|^+ = 3.9$ and then increases. This is in good agreement with Yao *et al.*'s (2017, 2018) DNS data where the spanwise body force was introduced to generate the LSSVs in a channel flow, resulting in a DR of 19 %. Their best control performance was achieved when $|\overline{W_{max}}|^+$ was approximately 4 times the friction velocity. They also proposed that the height of the maximum spanwise velocity y_c^+ should be around 30 for the effective merger of numerous velocity streaks in the near-wall region, which is consistent with the present results at y_c^+=24 (figure 9*b*). They achieved a DR of only 1.4 % at a small y_c^+ (= 5) since the wall jet was too thin to affect most parts of the streaks. So did they also at a large y_c^+ (= 80). They explained that the smaller, secondary vortices between the primary vortices and the wall became strong at a large y_c^+, leading to a stronger downwash which increases skin-friction drag.

3.6. *Local skin-friction drag variation*

As the plasma actuators generate LSSVs (figure 9), the local friction variation cannot be expected to be uniform along the spanwise direction. The friction may further recover downstream. It is important to document how the local friction varies along the z- and x-directions, which is crucial for us to understand the flow physics behind DR.

The local DR is measured downstream of the plasma actuators for configuration B along the z- and x-directions, based on the hot-wire-measured gradient of the streamwise velocity in the sublayer. Since the actuators cannot withstand a high E for a long time, the hot-wire measurements are then performed at $E = 4.25$ kV$_{p-p}$ and limited to only behind one half of the middle actuator pair, assuming a spanwise periodic variation in the DR. This assumption is reasonable because the two LSSVs generated by one pair of plasma actuators are statistically identical (figure 9). As such, the spanwise distribution of the local DR is expected to be symmetric about the centreline, i.e. $z^+ = 0$, between one pair of actuators and, for this reason, the data points are mirrored from the right to the left of $z^+ = 0$ (figure 14*a*), providing an overall view for the variation of DR. The local DR

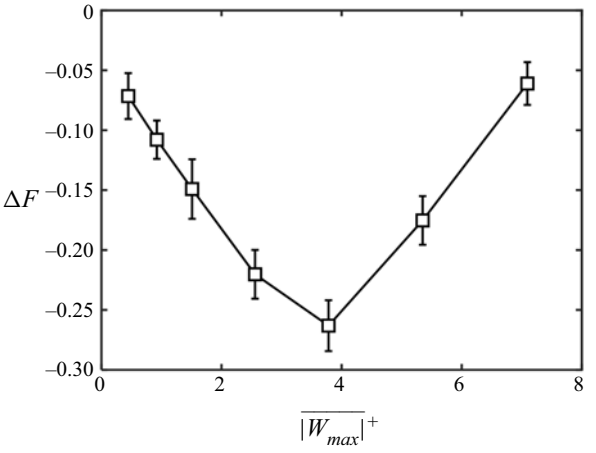

Figure 13. Dependence of the FE-force-balance-measured drag change ΔF on the mean maximum spanwise velocity $|\overline{W_{max}}|^+$ captured in the y–z plane (configuration B). The error bars denote the standard deviation of six repeats.

is measured at thirteen representative spanwise locations and ten streamwise positions, of which seven are over the FE and three are downstream of the FE. In figure 14, the local friction DR $\Delta\tau_w$ is given by $[(\overline{\tau_w})_{on} - (\overline{\tau_w})_{off}]/(\overline{\tau_w})_{off}$, where $(\overline{\tau_w})_{on}$ and $(\overline{\tau_w})_{off}$ are the time-averaged WSS with and without plasma control, respectively, estimated from the streamwise velocity gradient in the sublayer.

Figure 14(*a*) shows that the spanwise distributions of $\Delta\tau_w$ are qualitatively the same for different streamwise locations and may be divided into three distinct regions – namely, the drag increase region (R1), the pronounced DR region (R2) and the drag recovery region (R3). In Region R2 ($-160 < z^+ < -75$ and $75 < z^+ < 160$), the maximum DR is as high as 46 % at $x^+ = 167$, which corresponds spatially to the upwash of the LSSVs, as is evident in the PIV-measured time-averaged vorticity contours and velocity vectors in the y–z plane (Plane 4, figure 15). The low-speed fluid is lifted up from the wall, decreasing the streamwise velocity gradient near the wall, thus resulting in substantial DR. On the other hand, Region R1 occurs on the downwash side of the LSSVs, where the high-speed fluid is brought closer to the wall. The downwash of the high-speed fluid increases the streamwise velocity gradient near the wall and hence $\Delta\tau_w$. Therefore, there is a significant drag increase, i.e. $\Delta\tau_w > 0$, up to $x^+ = 415$ (figure 14*b*). These observations and inferences are consistent with those of Jeong *et al.* (1997) and Yao *et al.* (2017). Beyond $x^+ = 415$, the LSSVs become rather weak and shifted away from the wall (figure 15), and $\Delta\tau_w$ remains zero. Region R3 corresponds to an almost unchanged DR of approximately 23 % over $-75 < z^+ < 75$ at $x^+ = 167$. As will be seen later from flow visualization, the near-wall streaks in this region are stabilized as a result of the reduced meandering (Schoppa & Hussain 2002) which is modulated by the LSSVs. Similar spanwise distribution of local DR could also be found in the results of Iuso *et al.* (2002) and Canton *et al.* (2016*a*).

The streamwise recovery of $\Delta\tau_w$ is closely linked to the development of LSSVs, which (Plane 1 of figure 15) are generated right above the electrodes (figure 2*b*). These vortices grow in both strength and size when developing downstream from Plane 1 ($x^+ = -889$) to Plane 3 ($x^+ = 0$) due to the continually injected momentum by the plasma actuators, leading to a spatial evolution in the local DR over the actuators. This evolution, however, cannot be measured presently. Behind the actuators, the vortices grow very slowly in size

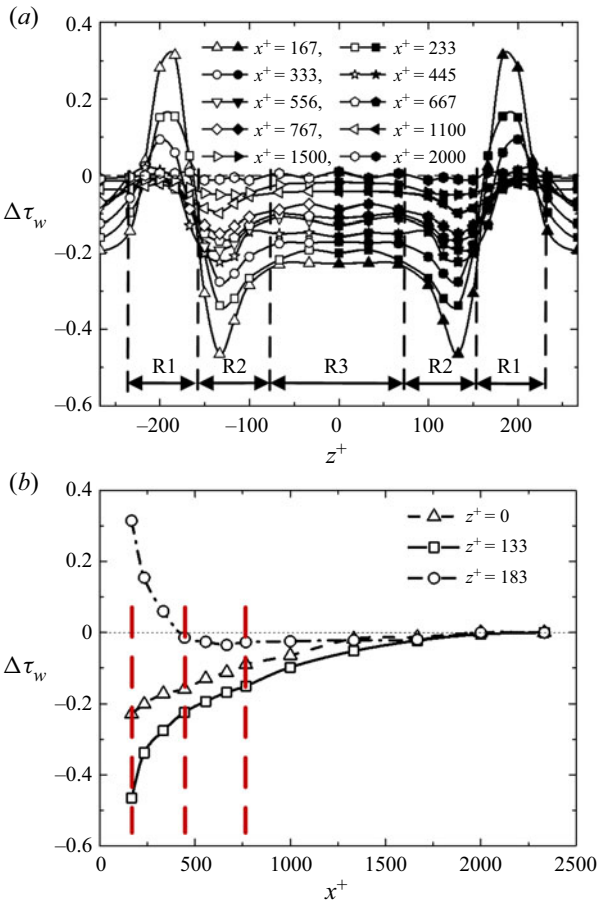

Figure 14. (*a*) Spanwise distributions of the local DR $\Delta\tau_w$ at 10 streamwise locations. The solid symbols denote the hot-wire-measured points while the open symbols denote the symmetrized points to give a direct view of local DR distribution downstream from the middle actuator pair. (*b*) Streamwise distributions of $\Delta\tau_w$ at three representative locations, i.e. $z^+ = 0$, 133, 183. Configuration B: $E = 4.25$ kV$_{p\text{–}p}$. The red vertical dashed lines denote the locations of the PIV measurement Planes 4, 5 and 6 in figure 15.

but decay rapidly in strength, perhaps due to cross-diffusion as well as viscous dissipation. The observation is consistent with the streamwise recovery of $\Delta\tau_w$. In figure 14(*b*), $\Delta\tau_w$ in Region R2 or R3 is initially pronouncedly negative and recovers gradually to the value of the natural state with increasing x^+, while $\Delta\tau_w$ measured in Region R1 drops from a level significantly positive to negative at $x^+ = 415$ and then maintains below zero before approaching the natural state. Note that $\Delta\tau_w$ does not overshoot, i.e. becoming positive, after reaching zero beyond $x^+ = 2000$. This is different from the drag recovery controlled by LSSVs in Iuso *et al.* (2002), where additional mass was introduced into the flow.

The strength (quantified by the plasma-generated vorticity in the time-averaged PIV measurements) of LSSVs decays rapidly as shown in the Planes 3 to 6 of figure 15, while the drag recovers relatively slowly downstream to its natural state. At $x^+ = 767$, the maximum vorticity is negligibly small (Plane 6, figure 15), while the corresponding maximum local DR remains as high as 20 % at $z^+ = 133$. This indicates that the low-drag state may persist even after the LSSVs vanish, which is consistent with Schoppa & Hussain's (1998) finding of the persistence of the low-drag state even upon sudden and

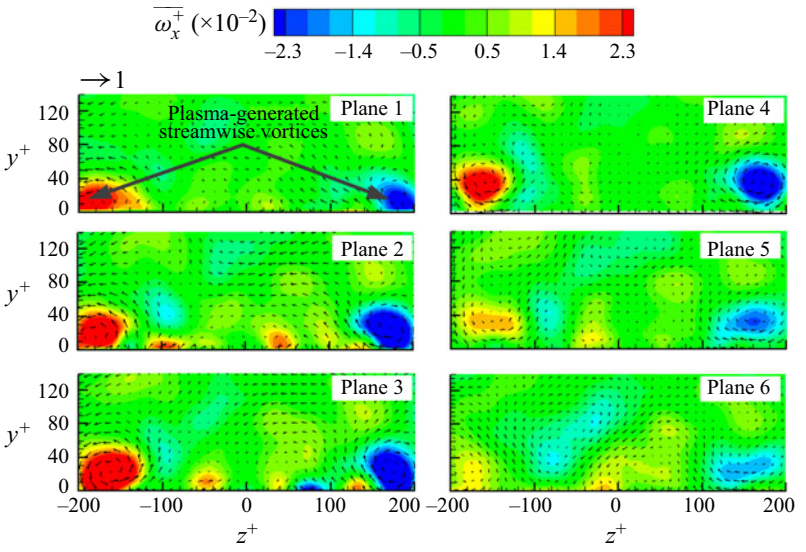

Figure 15. Time-averaged vorticity $\overline{\omega_x^+} = \overline{\mathrm{d}V^+/\mathrm{d}z^+} - \overline{\mathrm{d}W^+/\mathrm{d}y^+}$ and velocity vectors ($\overline{V^+}$, $\overline{W^+}$) in the y–z planes at $x^+ = -889$, -444, 0, 167, 433, 767. Configuration B: $E = 4.25$ kV$_{\mathrm{p-p}}$.

complete termination of the spanwise control flow. Schoppa & Hussain (1998) estimated the drag recovery distance of approximately 16 000 wall units by multiplying the relaxation time Δt^+ (in an order of 1000) of the controlled flow with the centreline flow velocity. If the same formula is used, the drag recovery distance would be $(U_\infty^+)(\Delta t^+) \sim 23\,000$ wall units in our case, much larger than the presently observed 2000 wall units. Two factors may account for the difference. Firstly, the LSSVs induced are structurally different in wall-jet profiles between the two studies. The LSSVs in Schoppa & Hussain (1998) collide with each other, with the maximum spanwise velocity at $H/2$ (H is the channel half-width), corresponding to approximately 80 wall units away from the wall. In contrast, the LSSVs generated by present configuration B do not collide and the maximum spanwise velocity occurs at $y^+ = 24$, implying a stronger interaction between the vortices and also with their image vortices (discussed earlier). Secondly, the real controlled flow may recover sooner than the estimation from $(U_\infty^+)(\Delta t^+)$. Iuso *et al.* (2002) experimentally introduced jet-induced LSSVs in a channel flow, and found a drag recovery distance of 9000 wall units, far less than that ($\sim$18 000 wall units) calculated from $(U_\infty^+)(\Delta t^+)$, even with a large control jet velocity ($100u_\tau$). The present spanwise velocity is less than u_τ, about 0.92 u_τ, at $E = 4.25$ kV$_{\mathrm{p-p}}$ (figure 13). Therefore, the difference may not be surprising.

The spanwise-averaged DR at each x^+ could be determined from spanwise integration of the hot-wire-measured local DR. The three pairs of plasma actuators in configuration B are identical (figure 16*a*). Note that the spanwise distribution of local $\Delta\tau_w$ downstream of the side actuator pair ($z^+ = -800 \sim -534$ or 534–800) differs from that behind the middle ($z^+ = 0$–267). Obviously, the LSSVs behind the middle may interact on both sides with those generated by the adjacent actuator pairs. Those behind the left- or right-side actuator pair, however, interact only on one side with the LSSVs behind the middle pair. Indeed, as shown in figure 16(*b*), the distribution of $\Delta\tau_w$ behind the right-side actuator pair ($z^+ = 534$–800) exhibits a considerable difference from that behind the middle pair ($z^+ = 0$–267) at $x^+ = 167$ and 767, which correspond to the most upstream and most downstream locations of the hot-wire-measured $\Delta\tau_w$ data over the FE, respectively. The vertical pink dashed line denotes the spanwise position of the actuator edge at $z^+ = 767$.

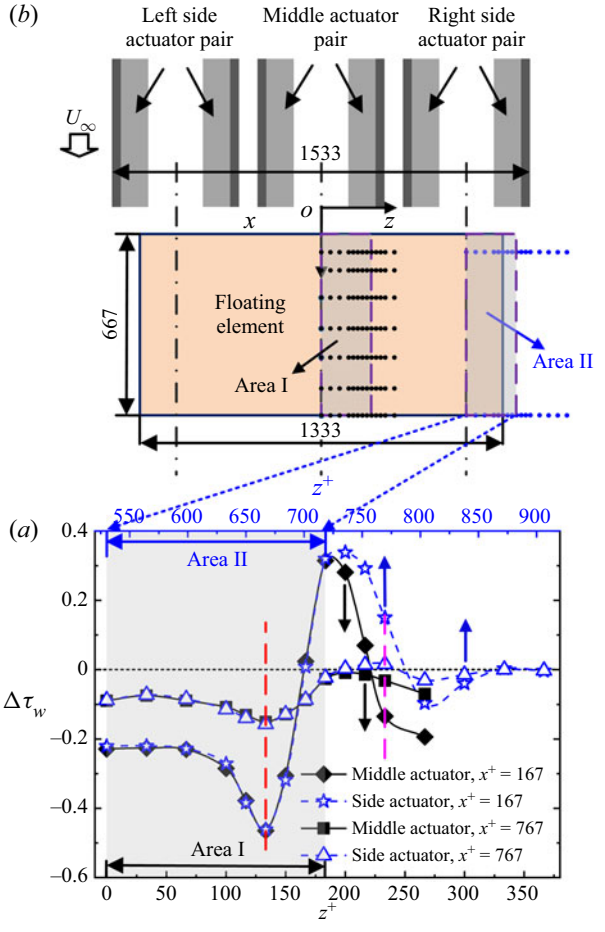

Figure 16. (*a*) Schematic of hot-wire measurement locations over the FE area denoted by black and blue symbols. (*b*) Comparison between the spanwise distributions of hot-wire-measured local DR $\Delta\tau_w$ at $x^+ = 167$ and 767, behind the middle and side pairs of actuators. The vertical red and pink dashed lines at $z^+ = 667$ and 767 denote the spanwise edges of FE and the right-side actuator pair, respectively.

Evidently, $\Delta\tau_w$ is appreciably non-zero until $z^+ \approx 867$ due to the stabilized streaks under the influence of the plasma-generated LSSVs. Nevertheless, the distribution of $\Delta\tau_w$ over $z^+ = 533$–716 (behind the right-side actuator pair) collapses completely with that over $z^+ = 0$–183 (behind the middle pair). That is, the distribution of $\Delta\tau_w$ in Area II is identical to that in Area I (figure 16*a*). Therefore, for $167 \leq x^+ \leq 767$, the distribution of $\Delta\tau_w$ downstream of the left- and right-side actuator pair over the FE area may be represented by that downstream of the middle actuator pair due to symmetry and periodicity. The spanwise-averaged drag change at a given streamwise location is then given by

$$\langle \Delta\tau_w \rangle_z = \frac{\int_{z_1^+}^{z_2^+} \Delta\tau_w \, \mathrm{d}z}{z_2^+ - z_1^+}, \tag{3.2}$$

where $\langle\,\rangle_z$ denotes spanwise-averaging, z_1^+ and z_2^+ are -667 and 667, corresponding to the spanwise edges of the FE. Thus calculated $\langle \Delta\tau_w \rangle_z$ is presented in figure 17, along

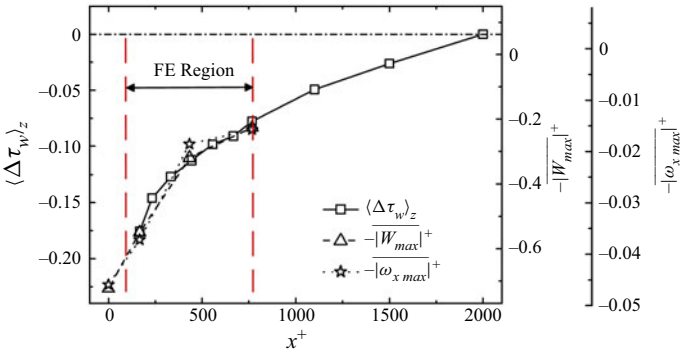

Figure 17. Variation of spanwise-averaged DR $\langle \Delta\tau_w \rangle_z$ (□), the negative maximum mean spanwise velocity $-|\overline{W_{max}}|^+$ (Δ) and negative maximum mean streamwise vorticity $-|\overline{\omega_{xmax}}|^+$ (☆) along the x^+ direction. Configuration B: $E = 4.25$ kV$_{p\text{–}p}$.

with $-|\overline{\omega_{xmax}}|^+$ and $-|\overline{W_{max}}|^+$. The $|\overline{\omega_{xmax}}|^+$ and $|\overline{W_{max}}|^+$ values are the peaks of the streamwise vorticity and the spanwise velocity, respectively, in the time-averaged vorticity and velocity at $x^+ = 0$, 167, 433, 767 (Planes 3, 4, 5 and 6 in figure 15) out of 1500 PIV images. When appropriately scaled, the variations of $|\overline{\omega_{xmax}}|^+$ and $|\overline{W_{max}}|^+$ in x are quite similar to each other. Both $-|\overline{\omega_{xmax}}|^+$ and $-|\overline{W_{max}}|^+$ rise with increasing x^+ due to the decay of the LSSVs, which is closely correlated with the increasing $\langle \Delta\tau_w \rangle_z$. We estimate, based on this correlation (figure 17), $\langle \Delta\tau_w \rangle_z$ at $x^+ = 0$ (the trailing edge of the plasma actuators) to be $-22\,\%$, where the hot-wire measurement is not possible. The streamwise integration of $\langle \Delta\tau_w \rangle_z$ (figure 17) from $x = 15$ to 115 mm or $x^+ = 100$ to 767 yields the DR on the FE-force balance measurement area of 100×200 mm^2 or 667×1333 wall units, viz.

$$\langle \Delta\tau_w \rangle_{xz} = \frac{\displaystyle\int_{x_1^+}^{x_2^+} \langle \Delta\tau_w \rangle_z \, \mathrm{d}x}{x_2^+ - x_1^+}, \tag{3.3}$$

where $\langle\,\rangle_{xz}$ denotes the spatial average along both z and x directions, and x_1^+ and x_2^+ are 100 and 767, respectively. The value of $\langle \Delta\tau_w \rangle_{xz}$ is found to be $-12.0\,\%$ at $E = 4.25$ kV$_{p\text{–}p}$, whilst the FE-force balance-measured DR is $-10.8\,\%$ (figure 10*a*). The difference in the DR between the hot-wire and force balance measurements may result from the experimental uncertainties of the two techniques. As shown in figure 10(*a*), the uncertainty of the force-balance-measured DR under $f = 11$ kHz, $E = 4.25$ kV$_{p\text{–}p}$ is $1.6\,\%$, which is larger than the difference ($1.2\,\%$) in the DR between the two measurements. Note that the spanwise-averaged DR drops along the streamwise direction, as shown figure 17, implying that the fully developed value of the DR at the trailing edge of the actuators, where the strength of the plasma-generated streamwise vortices is the maximum, would be larger than that measured by the FE-force balance.

In order to estimate the 'total' DR downstream of the actuators, $\langle \Delta\tau_w \rangle_z$ is integrated from $x^+ = 0$ to 2000 (figure 17), yielding $\langle \Delta\tau_w \rangle_{xz} = -7.12\%$. Note that the DR over the FE at $E = 5.75$ kV$_{p\text{–}p}$ is 2.5 times that at $E = 4.25$ kV$_{p\text{–}p}$ (figure 10*a*). For the same drag recovery rate, the DR area would be extended much larger than $x^+ = 2000$. Evidently, the DR area exceeds greatly that achieved by some other techniques. For instance, the drag recovers fully at $x^+ = 160$ for Bai *et al.*'s (2014) wall-normal oscillation technique.

4. Modified flow structure and DR mechanism

4.1. *Mean and r.m.s. streamwise velocities*

Mean streamwise velocity profiles normalized by both local inner and outer scales are presented in figure 18. In the absence of control, the $\overline{U^+}$ profile collapses well with that reported by Ricco & Wu (2004), showing a linear near-wall region for $y^+ < 5$ and a log region for $30 < y^+ < 170$. Under control, the $\overline{U^+}$ profile still follows $\overline{U^+} = y^+$ in the near-wall region, while the log region shifts upwards or downwards, depending on the local drag change. At $z^+ = 133$ (Region R2) and 0 (Region R3), where the local WSS is reduced, there is the expected upward shift of the log layer for increased DR (figure 18*a*,*c*). This is consistent with the results of Ricco & Wu (2004), who experimentally investigated the spanwise wall oscillation in the TBL and achieved the maximum DR of 32 %. Note that the slope of the $\overline{U^+}$ profile in the log-law region in Ricco & Wu (2004) is identical to the uncontrolled flow, as the mean streamwise velocity is affected only for $y^+ < 30$ and the shift of the log region results directly from the reduced friction velocity used for normalization. A similar phenomenon is also observed in the present study at $z^+ = 0$. However, at $z^+ = 133$, corresponding to the maximum DR location, the slope of the $\overline{U^+}$ profile increases compared with the uncontrolled flow due to the strong upwash of the LSSVs. On the other hand, at $z^+ = 183$ in Region R1, the local drag increases and the logarithmic region shows the expected downward shifts. The streamwise velocity profiles normalized by outer scales may give an intuitive view of the changes as the boundary layer thickness and the free-stream velocity are unchanged under control. There is a distinct deficit of $\bar{U}/U_\infty$ in the near-wall region at $z^+ = 133$ and 0 (the insets in figure 18*d*,*f*), which is consistent with the measured DR in these locations. In comparison, $\bar{U}/U_\infty$ at $z^+ = 183$ under control is larger than without control in the near-wall region. At $z^+ = 133$ where the largest DR is achieved, the strong upwash due to LSSVs may produce a change in $\bar{U}/U_\infty$ over $y/\delta = 0$–0.29 (figure 18*d*). In other words, almost the entire log-law region is affected by the control, which accounts for the increased slope of the $\overline{U^+}$ profile in the region (figure 18*a*). At the other two locations ($z^+ = 0$ and 183), the changes in the velocity profile are limited to $y/\delta < 0.04$.

Figure 19 presents the u_{rms} profiles, normalized by both local inner and outer scales. At $z^+ = 133$ in Region R2, u^+_{rms} changes little for $y^+ < 3$ under control. However, u^+_{rms} increases rapidly, exceeding that of the uncontrolled flow, away from the wall until $y^+ = 220$, due to the perturbation by the LSSVs. Yao *et al.* (2018) made a similar observation and attributed the increased u^+_{rms} to the advection of the externally introduced LSSVS, which could transport the near-wall turbulence and the QSVs to the outer flow. The movement of these structures is also reflected in the altered wall-normal location of u^+_{rms}, which moves away from $y^+ = 14$ to 19. Tardu (2001) proposed that DR be achievable by pushing the QSVs away from the wall or decreasing their intensity. The upward movement of the QSVs is consistent with the observed DR. Similar phenomenon is also found at $z^+ = 0$, albeit with smaller u^+_{rms}. At $z^+ = 183$ in Region R1, u^+_{rms} is always smaller under control than without control for $y^+ < 35$, as noted by Canton *et al.* (2016*a*) in their DNS data, where the spanwise body force was introduced to generate LSSVs in a turbulent channel. Note that at $z^+ = 133$ (figure 19*a*) the u^+_{rms} profile under control does not collapse with that in the natural flow for $y^+ > 300$, which is attributed to the normalization of y by the local wall variables (Bai *et al.* 2014), not to control. The y extent of control-affected region could be inferred in outer-scaled plot (figure 19*d*–*f*). At all three spanwise locations, u_{rms}/U_∞ with and without control collapse beyond 0.29δ. It is noteworthy that the variations of u_{rms} in outer scales are almost opposite to that in inner

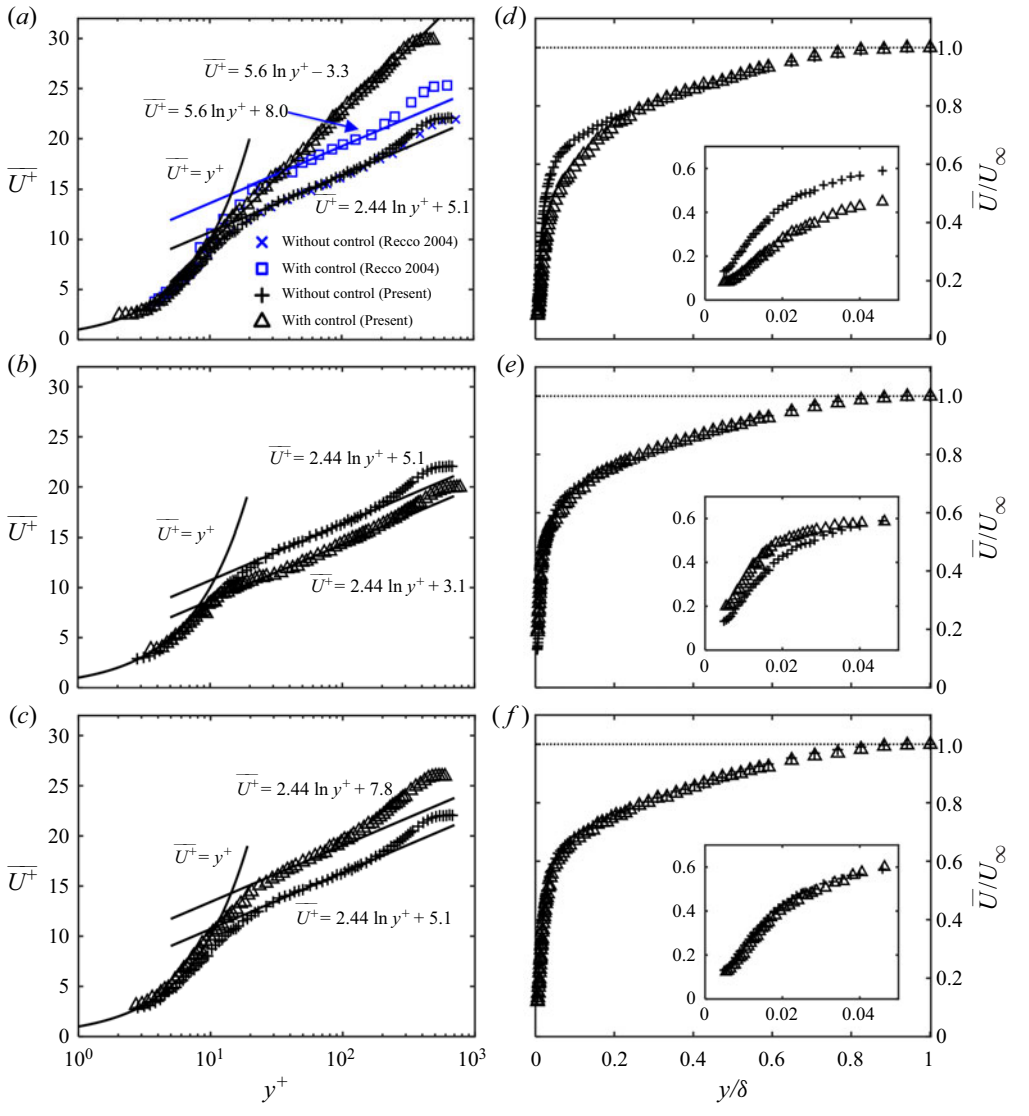

Figure 18. Mean streamwise velocity $\overline{U^+}$ profiles in (*a–c*) inner and (*d–f*) outer scales (configuration B: $E = 4.25$ kV$_{p\text{–}p}$); (*a*,*d*) $(x^+, z^+) = (167, 133)$, (*b*,*e*) (167, 183), (*c*,*f*) (167, 0). The insets in (*d–f*) are the zoom-in views of the near-wall region.

scales in the near-wall region. For example, although u^+_{rms} increases within $3 < y^+ < 12$ at $z^+ = 0$ and 133 under control, u_{rms} is even lower than in the uncontrolled case (the insets in figure 19*d*,*f*) as a direct result of the lift up of the QSVs by the upwash effect of the LSSVs. Yet, the inner scales, i.e. u_τ and δ_ν, change considerably under control due to substantial local DR, causing an increase in u^+_{rms}.

4.2. *Visualized flow structure*

The flow structure modification under control is well captured by the smoke-wire flow visualization in two x-z planes at $y^+ = 20$ and 50, as shown in figures 20 and 21,

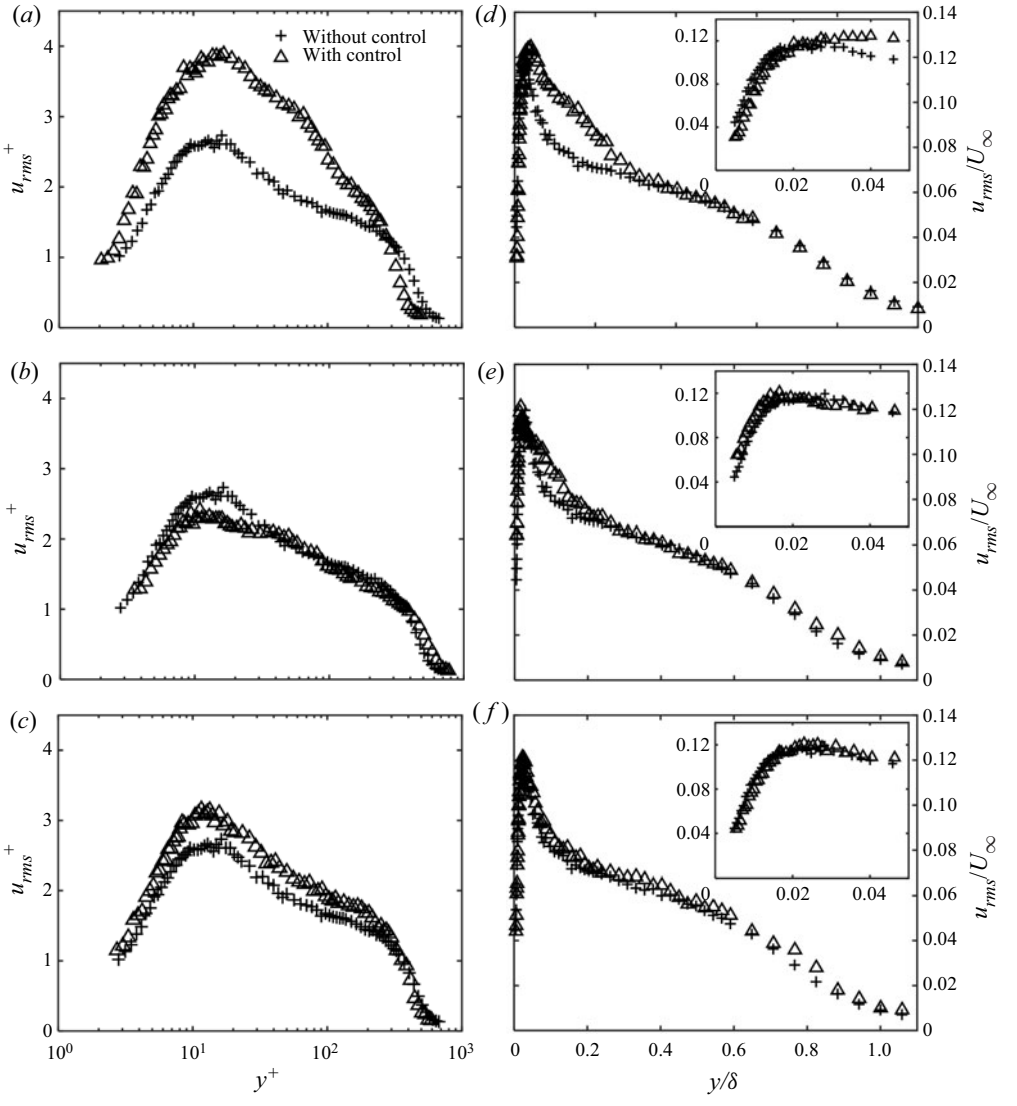

Figure 19. Profiles of the r.m.s. value of fluctuating velocity u normalized by their local (*a–c*) inner and (*d–f*) outer scales (configuration B: $E = 4.25\ \mathrm{kV_{p\text{–}p}}$); (*a,d*) $(x^+, z^+) = (167, 133)$, (*b,e*) (167, 183), (*c,f*) (167, 0). The insets in (*d–f*) show the near-wall region.

respectively. Attempts were also made for $y^+ < 20$, though unsuccessful because the smoke-wire burned out easily due to the high voltage needed for plasma actuators. The value of U_∞ was chosen at $1.8\ \mathrm{m\ s^{-1}}$ to capture the flow visualization images of good quality. At the height of $y^+ = 20$, smoke filaments originating from the smoke-wire, placed at $y^+ = 17$, rise and track the organized motions or QSVs, forming the low-speed streaks, and are illuminated by the x–z laser sheet at $y^+ = 20$. On the other hand, the high-speed fluid is swept by vortices, resulting in high-speed streaks, which contain no seeding particles to be illuminated by the laser sheet. In the absence of control, the low- and high-speed streaks take place side by side alternately, and they occur rather randomly in both space and time. The spanwise spacing between low-speed streaks is approximately

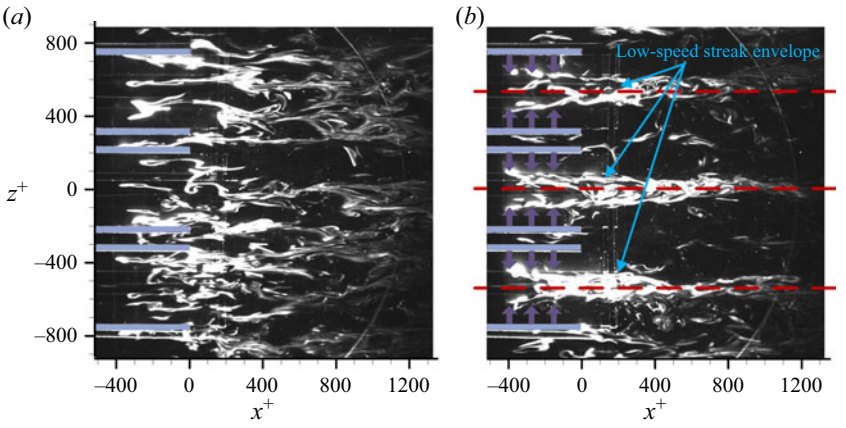

Figure 20. Smoke-wire flow visualization of instantaneous flow structure in the x–z planes. (*a*) Uncontrolled; (*b*) under control (configuration B: $E = 5.75$ kV$_{p\text{–}p}$). The smoke-wire and the laser sheet are positioned at $y^+ = 17$ and 20, respectively. Flow at $U_\infty = 1.8$ m s^{-1} is left to right. The red dashed lines indicate the centrelines of the actuator pairs. The horizontal blue-coloured bars and the vertical arrows represent the upper electrodes of the plasma actuators and the ionic wind direction, respectively.

$100\delta_\nu$, which is consistent with the literature (e.g. Kline *et al.* 1967; Schoppa & Hussain 2002; Bai *et al.* 2014). Once the control is applied, the streaks change greatly, becoming more organized and stabilized due to the LSSVs, as shown in figure 20(*b*). The illuminated, white-coloured low-speed streaks are all pushed into the central region of each actuator pair by the wall jets. These streaks merge, forming a streak envelope. Meanwhile, the darker high-speed fluid lies between the low-speed streak envelopes due to the downwash of the LSSVs. A similar observation is made by Yao *et al.* (2018) based on the DNS data in a channel flow, where many low-speed streaks merged under the influence of spanwise-opposed wall jets (Schoppa & Hussain 1998). The altered flow structures are in distinct contrast with those under the spanwise wall-oscillation control in Choi, Debisschop & Clayton (1998) and Karniadakis & Choi (2003). Under the spanwise wall oscillation, the natural streaky structures are tilted away from the mean flow direction at the leading edge of the oscillating plate. They proposed that the negative spanwise vorticity was generated during the spanwise wall oscillation and, as a result, the streamwise velocity in the near wall of the TBL was reduced, accounting for the friction DR.

In the absence of control, the streaks in the plane of $y^+ = 50$ (figure 21) are more meandered and chaotic than those at $y^+ = 20$, due to the weak ejection and sweep motions in the lower part of the log region (Kline *et al.* 1967). Under control, the streaks are pushed toward the centreline of the actuator pairs, like the case at $y^+ = 20$, although exhibiting more meandering motions. The occurrence of the more meandering streaks results from upwash of QSVs by LSSVs, also producing increased u^+_{rms} in this region. From a different perspective, consider the turbulence regeneration cycle proposed by Kim (2011) and Schoppa & Hussain (2002). The near-wall streaks are generated from the fluid lift-up by the QSVs (Jeong *et al* 1997; Jimenez & Pinelli 1999). These streaks are unstable to both the normal-mode instability (Hamilton, Kim & Waleffe 1995) and particularly the non-normal-mode instability, namely, transient growth (Schoppa & Hussain 2002), resulting in the streamwise-dependent spanwise flow disturbances which are necessary to generate new QSVs. Using DNS, Schoppa & Hussain (2002) demonstrated that the normal-mode streak instability could not cause significant vortex generation near the wall,

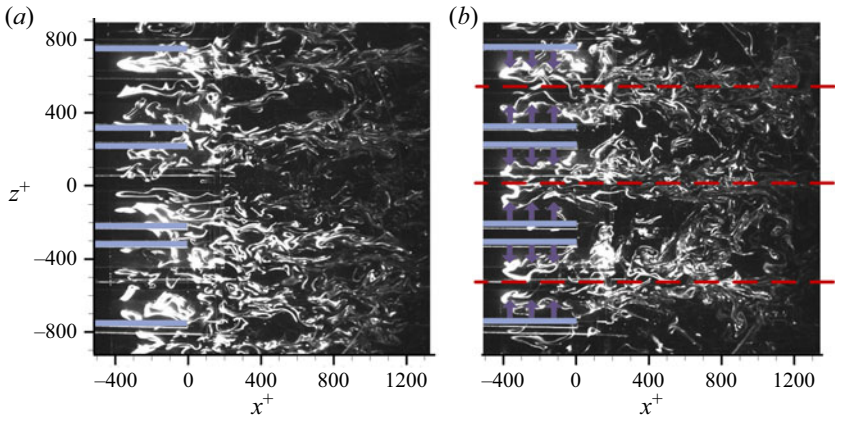

Figure 21. Smoke-wire flow visualization of instantaneous flow structure in the x–z planes. (*a*) Uncontrolled; (*b*) under control. The smoke-wire and the laser sheet are positioned at $y^+ = 47$ and 50, respectively. Please refer to figure 20 for flow conditions and legends.

due to a limited amplification (only twofold). They presented the streak transient growth mechanism, which is capable of producing much larger amplification (tenfold) of the x-dependent disturbances and accounts for the formation of a sheet of streamwise vorticity, which then leads to the generation of new QSVs via stretching by $\partial u/\partial x$ of the meandering streaks. In view of the stabilized streaks due to reduced streak flank angle under control, the generation of new QSVs is suppressed; therefore, the skin-friction drag is reduced significantly.

4.3. *Suppressed wall-normal vorticity*

A change in the streak transient growth is also reflected in the wall-normal vorticity ω_y because of the close association between this and ω_y (Schoppa & Hussain 2002; Kim 2011). Figure 22 presents the probability density function (PDF) of ω_y/ω_{yrms}, calculated from the PIV data captured downstream of the plasma actuators in the x–z plane of $y^+ = 24$. The calculation area is the same as the area of the FE. Once plasma control is applied, the probability of large ω_y/ω_{yrms} drops appreciably compared to that in the uncontrolled flow, while that of small ω_y/ω_{yrms} is significantly increased, indicating a decreased ω_y over the FE area. A similar result was also obtained by Iuso *et al.* (2002), who achieved a spanwise-averaged DR of 15 % in a turbulent channel flow using an array of inclined wall jets to induce LSSVs. The observed change in ω_y/ω_{yrms} implies stabilized streaks and the suppressed transient growth leading to fewer QSVs, hence the observed DR.

4.4. *Weakened bursting events*

The bursting events play an important role in the dynamics of the TBL and may be affected by DR. The events are detected from the hot-wire-measured fluctuating velocity signal by the variable-interval time-average (VITA) technique (Blackwelder & Kaplan 1976). Two important parameters, namely, the averaging duration T^+ and the threshold k, need to be carefully chosen to ensure the events to be correctly detected, where T^+ must be of the order of the time scale of the burst and k is such that the VITA value of the fluctuating velocity associated with a detected event is larger than ku_{rms}^2. Following Choi *et al.* (2011),

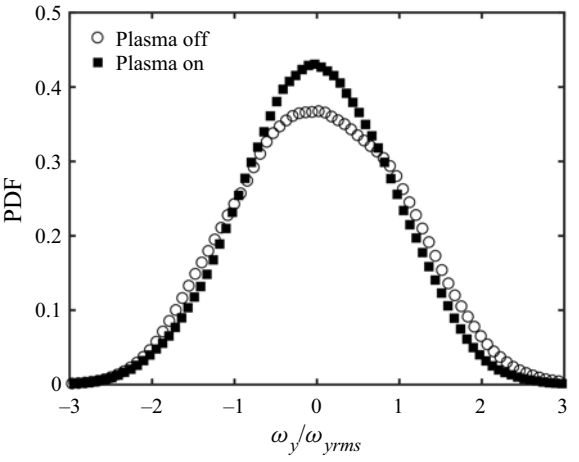

Figure 22. PDF of the normalized wall-normal vorticity ω_y/ω_{yrms} calculated from the PIV data obtained in the plane of $y^+ = 24$ with and without control (configuration B: $E = 4.25$ kV$_{p\text{–}p}$). The calculation area is the same as the area of the FE.

k and T^+ are set at 1 and 10, respectively. Figure 23(*a*) presents a comparison of the ensemble-averaged u^+, i.e. $\langle u^+\rangle_t$, between uncontrolled and controlled cases, where $\langle\,\rangle_t$ denotes the ensemble averaging based on the VITA detections. In the absence of control, $\langle u^+\rangle_t$ agrees reasonably well with Choi *et al.*'s (2011) data, which provides a validation for the present VITA analysis. When the plasma control is applied, the strength of the burst, i.e. the difference between the maximum and the minimum $\langle u^+\rangle_t$, contracts by 15 % (figure 23*a*) at $z^+ = 133$ (Region R2) compared to the uncontrolled case, indicating weakened bursting events. Similarly, the bursting event is also found to be impaired at $z^+ = 0$ (R3) – consistent with the suppressed u_{rms}/U_∞ at $y^+ = 5$ in Regions R2 and R3. On the other hand, there is a small increase (10 %) in the strength of the burst at $z^+ = 183$ (R1), where u_{rms}/U_∞ increases slightly at $y^+ = 5$ (figure 19*e*). The weakened burst event is an indication that the streaks are stabilized in the TBL (Bai *et al.* 2014), and thus the substantial DR. The slope $\mathrm{d}\langle u^+\rangle_t/\mathrm{d}t$ of the controlled flow at $z^+ = 0$ and 133 is slightly lower than that of the uncontrolled flow (figure 23*a*). As a rapid increase in $\langle u^+\rangle_t$ is directly linked to the sweep motion on the downwash side of the QSVs, the reduced $\mathrm{d}\langle u^+\rangle_t/\mathrm{d}t$ indicates weakened QSVs. A similar observation was also made by Iuso *et al.* (2002), who introduced LSSVs in the channel flow using inclined jets. Their VITA analysis suggested a reduced slope $\langle \tau_w\rangle_t/\mathrm{d}t$ of the controlled flow, which was ascribed to the suppressed near-wall longitudinal vortex regeneration by the stabilized streaks. As τ_w is closely correlated with the near-wall streamwise velocity, the reduced $\mathrm{d}\langle u^+\rangle_t/\mathrm{d}t$ is fully consistent with Iuso *et al.*'s (2002) VITA analysis. The value of $\langle u^+\rangle_t$ further indicates an enhanced ejection at $z^+ = 183$ (R1) compared to the uncontrolled flow, which seems to contradict the downwash of the plasma-induced LSSVs. As the VITA technique involves only the fluctuating velocity, the mean flow should not influence $\langle u^+\rangle_t$. Note that the $\langle u^+\rangle_t$ signal measured at $(x^+, y^+, z^+) = (167, 5, 183)$ under control and that at $(x^+, y^+, z^+) = (167, 15, 183)$ from the uncontrolled flow are quite similar to each other, as is evident in figure 23(*b*). As the ejection is closely related to the near-wall QSVs, its enhanced signature at $y^+ = 5$ results apparently from the motion of QSVs towards the wall under the downwash effect of LSSVs.

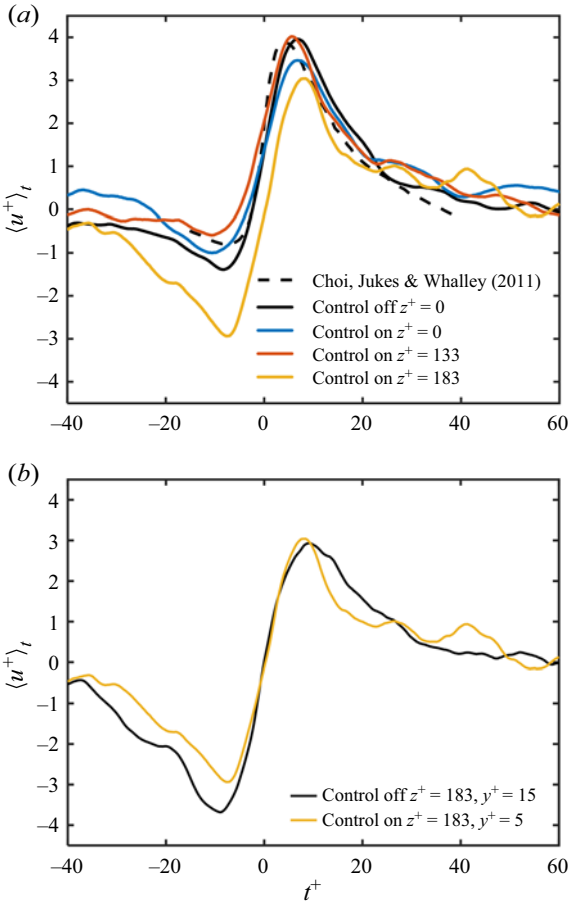

Figure 23. (*a*) Ensemble-averaged streamwise fluctuating velocity $\langle u^+\rangle_t$ based on VITA detection from hot-wire results. The angle bracket with subscript *t*, i.e. $\langle\,\rangle_t$, denotes the ensemble averaging based on the VITA detections. Ensemble averaging parameter: $k = 1$, $T^+ = 10$. Measuring location: $(x^+, y^+) = (167, 5)$. Control parameter: $E = 4.25$ $\mathrm{kV_{p\text{–}p}}$ (configuration B). (*b*) Comparison of $\langle u^+\rangle_t$ between the uncontrolled flow at $(x^+, y^+, z^+) = (167, 15, 183)$ and controlled flow at $(x^+, y^+, z^+) = (167, 5, 183)$.

4.5. *Dissipation and production of the TKE budget*

The dissipation and production are the dominant terms in the TKE budget near the wall (Pope 2001), and their changes may provide insight into the mechanism behind the DR. The dissipation ϵ is estimated through only one of its 12 components, i.e. $\overline{(\mathrm{d}u/\mathrm{d}y)^2}$, which accounts for nearly 80 % of the total dissipation in the viscous sublayer and 41 %–72 % in the buffer layer (Antonia, Kim & Browne 1991; Qiao, Xu & Zhou 2019). The standard uncertainty $s_{\overline{(\mathrm{d}u/\mathrm{d}y)^2}}$ of $\overline{(\mathrm{d}u/\mathrm{d}y)^2}$, is calculated as

$$s_{\overline{(\mathrm{d}u/\mathrm{d}y)^2}} = \sqrt{\left(\overline{(\mathrm{d}u/\mathrm{d}y)^2}\right)^2 + \left(\sqrt{2}\sigma_{\gamma_{\mathrm{d}u/\mathrm{d}y}}\overline{\gamma_{\mathrm{d}u/\mathrm{d}y}}\sqrt{1 + \frac{\sigma^2_{\gamma_{\mathrm{d}u/\mathrm{d}y}}}{2\overline{\gamma_{\mathrm{d}u/\mathrm{d}y}}^2}}\right)^2}\sqrt{\frac{2}{N_p}}, \tag{4.1}$$

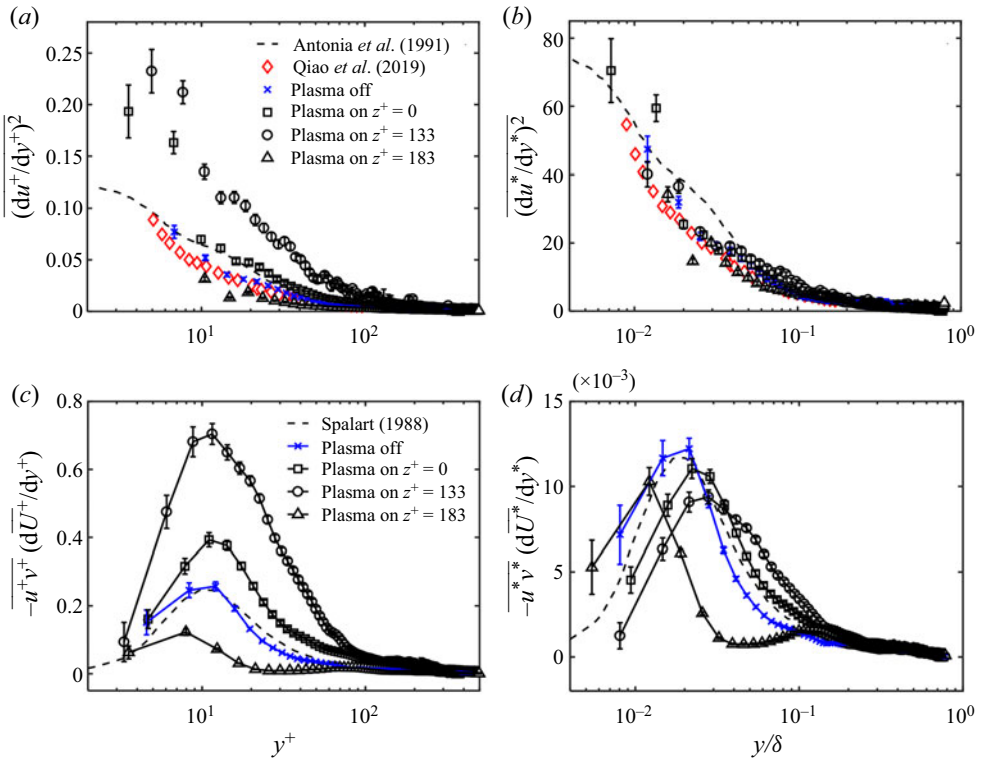

Figure 24. Profiles of $\overline{(du/dy)^2}$ (*a*,*b*) of the mean turbulent energy dissipation and production $-\overline{uv}(d\bar{U}/dy)$ (*c*,*d*) in inner scale (*a*,*c*) and outer scale (*b*,*d*), respectively. Control parameter: $E = 4.25$ kV$_{p\text{–}p}$ (configuration B); $x^+ = 167$.

where N_p is the number of PIV image pairs, $\gamma_{du/dy}$ is the measurement uncertainty of d*u*/d*y*, $\overline{\gamma_{du/dy}}$ and $\sigma_{\gamma_{du/dy}}$ are the time-averaged value and the standard deviation of $\gamma_{du/dy}$, respectively. The error bars in figure 24(*a*,*b*) are plotted as $1.96s_{\overline{(du/dy)^2}}$, which corresponds to a 95 % confidence interval. In the absence of control, $\overline{(du/dy)^2}$ agrees well with Qiao *et al.*'s (2019) measurement using a probe of two parallel hot-wires and reasonably well with Antonia *et al.*'s (1991) DNS data. Under control, the near-wall $\overline{(du^+/dy^+)^2}$ at $z^+ = 133$ and 0 in Regions R2 and R3, respectively, becomes much larger than that of the uncontrolled case. The greatly increased dissipation is consistent with the substantial DR (Qiao, Wu & Zhou 2018). The $\overline{(du^+/dy^+)^2}$ becomes smaller at $z^+ = 183$ in Region 1, where drag increases. However, $\overline{(du^*/dy^*)^2}$, normalized by the outer scales, with control deviates only slightly from that without control in all the three regions (figure 24*b*). Apparently, the variation in $\overline{(du^+/dy^+)^2}$ (figure 24*a*) with and without control is largely attributed to the difference in the scaling parameters, namely, local friction velocity and viscous length scale.

The measured turbulent energy production $-\overline{u^+v^+}(d\overline{U^+}/dy^+)$ in the absence of control (figure 24*c*) agrees reasonably well with Spalart's (1988) DNS data, albeit with a small departure. This departure is probably due to the limited spatial resolution of the PIV measurements, as reported in Mizumoto *et al.* (2012). The spatial resolution is 1 wall unit in the near-wall region for Spalart's (1988) data but 3.75 wall units (0.56 mm)

for our PIV data. The standard uncertainty s_P of the production term $-\overline{uv}(\mathrm{d}\bar{U}/\mathrm{d}y)$ is calculated through $s_P = \sqrt{(\overline{uv})^2 s^2_{\mathrm{d}\bar{U}/\mathrm{d}y} + (\mathrm{d}\bar{U}/\mathrm{d}y)^2 s^2_{\overline{uv}}}$, where $s_{\mathrm{d}\bar{U}/\mathrm{d}y}$ and $s_{\overline{uv}}$ are the standard uncertainties of $\mathrm{d}\bar{U}/\mathrm{d}y$ and $\overline{uv}$, respectively (Sciacchitano & Wieneke 2016). The error bars are plotted in figure 24(*c*,*d*) as 1.96 s_P, corresponding to a 95 % confidence interval. The maximum turbulent energy production is 0.25 at $y^+ \approx 14$ without control. Like $\overline{(\mathrm{d}u^+/\mathrm{d}y^+)^2}$, $-\overline{u^+v^+}(\mathrm{d}\overline{U^+}/\mathrm{d}y^+)$ goes up significantly at $z^+ = 133$ in Region R2 and $z^+ = 0$ in Region R3 but drops at $z^+ = 183$ in Region R1 (figure 24*c*). This is ascribed to the significantly changed local friction velocity and viscous length scale under control. For example, the friction velocity decreases from 0.105 m s^{-1} in no control to 0.077 m s^{-1} under control at $z^+ = 133$ in Region R2 and increases to 0.121 m s^{-1} under control at $z^+ = 183$ in Region R1. However, when normalized by the outer scales (figure 24*d*), $-\overline{u^*v^*}(\mathrm{d}\overline{U^*}/\mathrm{d}y^*)$ is substantially reduced near the wall for the two DR regions, though a slight increase is observed at $z^+ = 183$ in Region R1. Compared with the uncontrolled case, the peak of $-\overline{u^*v^*}(\mathrm{d}\overline{U^*}/\mathrm{d}y^*)$ retreats by approximately 26 %, 16 % and 10 % at $z^+ = 133$, 183 and 0, respectively. This retreat is fully consistent with the stabilized streaks (figure 20). The following discussion on production and dissipation will focus on the results normalized by the outer scales (figure 24*b*,*d*). Note that the location of peak TKE production changes once the control is applied. For instance, the TKE production peak at $z^+ = 133$ moves away from the wall due to the upwash of the plasma-generated LSSVs but shifts toward the wall at $z^+ = 183$ because of the downwash of the vortices (figure 24*d*). As the QSVs are responsible for the production of TKE in the TBL (Wallace 2016), this shift in the production peak suggests the movement/alteration of the QSVs by the LSSVs. At $z^+ = 133$ and 0, the QSVs are lifted away from the wall due to the upwash of the plasma-generated vortices, which also accounts for the DR (Tardu 2001). However, the energy production at $0.028 < y/\delta < 0.301$ $(16 < y^+ < 170)$ is increased compared to the uncontrolled case due to the lifted QSVs, which is also consistent with the increased u_{rms}/U_∞ in this region (figure 19*d*). At $z^+ = 183$, the downwash of the LSSVs pushes the QSVs towards the wall. Thus, the production is mostly confined to the near-wall region, accounting for an increased production for $y/\delta < 0.012$ $(y^+ < 7)$ but a reduced production further away for $y/\delta = 0.012$–0.109 $(y^+ = 7$–$60)$. A similar observation was also made from the DNS results of Mahfoze & Laizet (2017), who superimposed plasma-induced spanwise flow oscillation near the wall in a turbulent channel flow of relatively low Re_τ $(= 180)$. They achieved a DR of 24 % under the optimal control parameters. Accordingly, the TKE production peak was reduced by 19 %, with its location shifted away from the wall.

4.6. *DR mechanism*

A DR mechanism is proposed based on the distribution of the local DR and the various aspects of the flow captured with and without control. The key strategy of the present plasma control is to manipulate the near-wall coherent structures, which are accountable for the high skin friction in the TBL. It has been well established that the near-wall turbulence regeneration cycle plays a crucial role in the sustenance of the coherent structures (e.g. Kim 2011). As such, interrupting this cycle may lead to substantially weakened near-wall coherent structures, resulting in a reduction in the skin friction. Several DR techniques for the TBL have been developed based on this concept, including spanwise wall oscillation (e.g. Choi *et al*. 1998; Agostini, Touber & Leschziner 2014) or a spanwise/transverse or streamwise-travelling wave (e.g. Du *et al*. 2002; Quadrio *et al*. 2009; Bai *et al*. 2014; Qiao *et al*. 2017).

In present study, the plasma actuators generate counter-rotating LSSVs (figure 15). These 'externally' introduced vortices and their associated spanwise wall jets act to merge the streaks. As a result, the streaks are broader and have reduced meandering (figure 20), which is also reflected by the reduced wall-normal vorticity ω_y (figure 22) – both explained by Schoppa & Hussain (2002). The streaks are pushed into the central region of each actuator pair by the plasma-generated spanwise flow, and moved away from the wall by the upwash motion of these external vortices (figure 20). All the observations along with the comparison in the bursts between the controlled and uncontrolled flows (figure 23) point to the substantially stabilized streaks (Yao *et al.* 2018).

The instability of streaks, especially that due to the transient growth, is the essential element for the generation of QSVs (Schoppa & Hussain 2002; Kim 2011) in the turbulence regeneration cycle. Naturally, the stabilized streaky structures will interrupt this cycle and subsequently suppress the generation of new QSVs, leading to weakened near-wall coherent structures, which is confirmed from the reduced turbulence intensity and TKE production in Regions R2 and R3 (figures 19 and 24*d*). The weakened QSVs and merged streaks under the control of externally generated LSSVs are also observed in Yao *et al.*'s (2018) DNS and Iuso *et al.*'s (2002) experiments. As a result, the skin friction is substantially reduced (figure 14). Interestingly, these LSSVs change little the turbulent energy dissipation (figure 24*b*), unlike some other techniques such as the piezo-ceramic-actuator-generated spanwise-travelling wave (Bai *et al.* 2014; Qiao *et al.* 2017) where the enhancement of the dissipation in the near-wall region is one of the keys for DR.

5. Conclusions

A TBL at $Re_\theta = 1450$ is experimentally manipulated using a spanwise array of longitudinal plasma actuators with a view to reducing skin friction and understanding the flow physics. Three DBD plasma-actuator configurations are explored, and the resulting DR is captured using an in-house built, precision FE-force balance. Extensive hot-wire, PIV and flow visualization measurements are done with and without control. Following conclusions are drawn.

(a) The developed FE balance is characterized by following features: (i) the same pressure on the upper and lower surfaces of the FE, (ii) negligible local flow separation from the gap surrounding the FE, effectively avoiding any additional forces on the FE, (iii) negligibly small moment about the FE centre due to the pressure distribution on the surface and (iv) negligibly small misalignment between the FE and the flat plate. As such, this balance overcomes the major problems of the conventional FE balance (Hakkinen 2004), providing reliable measurements. Furthermore, a novel calibration method is developed based on the μ-PTV-measured *in situ* local skin-friction drag. As a result, this balance resolves accurately the skin-friction drag of the order of 10^{-4} N, much smaller than that (10^{-1} N) of Krogstad & Efros (2010).

(b) Three plasma-actuator configurations have been investigated for reducing the skin-friction drag. Both configurations A and B produce arrays of counter-rotating LSSVs, albeit with a difference in downstream development. On the other hand, configuration C produces co-rotating LSSVs. B always outperforms A in terms of DR and control efficiency since collision of the plasma-generated vortices in A adversely affects the streak transient growth, giving rise to an additional disturbance across the TBL and thus produces less DR. DR of C is much lower than that of

A or B because, given the same voltage E, the neighbouring co-rotating LSSVs in C interact with each other (figure 9*c*), which adversely affect their strength.

(c) Configuration B, investigated in detail, shows that DR is more pronounced with increasing spanwise velocity $|\overline{W_{max}}|^+$ until $|\overline{W_{max}}|^+$ reaches 3.9. The occurrence of this optimal $|\overline{W_{max}}|^+$ is fully consistent with Schoppa & Hussain's (2002) and Yao *et al.*'s (2017) observation. At $E = 4.25$ kV$_{p–p}$, the drag recovery is rather rapid from $x^+ = 0$ to 333 and is approximately linear further downstream until recovery at $x^+ \approx 2000$ (figure 14), beyond which no drag increase is observed. The drag recovery distance may greatly exceed 2000 wall units at the optimal $E = 5.75$ kV$_{p–p}$ where DR on the FE is 2.5 times that at $E = 4.25$ kV$_{p–p}$. The maximum DR achieved is 26 % on the FE (667 × 1333 wall units). When E is beyond the optimum value, DR decreases and could even change to a drag increase as the vortices grow rapidly and lead to an increase of coherent shear stress, which produces additional drag in the TBL (Yao *et al*. 2018).

(d) There has been a pronounced change in the flow structure up to $y^+ \approx 170$ ($y/\delta = 0.29$) for configuration B. The u_{rms}/U_∞ decreases appreciably at $y/\delta < 0.024$ ($y^+ < 14$) in the DR region. Flow visualization confirms that streaks are stabilized by the LSSVs. As the instability/transient growth of the streaks causes QSVs in the TBL (Schoppa & Hussain 1998, 2002), the stabilized streaks imply a drop in the generation of new QSVs, which is supported by an appreciably reduced wall-normal vorticity and a decrease in the strength of the near-wall bursting events. As a result, the TKE production is decreased substantially for $y/\delta < 0.024$ ($y^+ < 14$) under control, even for Region R1 where drag is increased – which is internally consistent with the decreased u_{rms}/U_∞ near the wall in Regions R2 and R3. On the other hand, dissipation changes little under control.

Funding. Authors wish to acknowledge support given to them from NSFC through grants 11632006, 91752109, 91952204, 51935005 and from Research Grants Council of Shenzhen Government through grants JCYJ20150513151706565 and JCYJ20160531193045101.

Declaration of interests. The authors report no conflict of interest.

Author ORCIDs.
X.Q. Cheng http://orcid.org/0000-0002-6211-210X;
F. Hussain http://orcid.org/0000-0002-2209-9270;
W. Schröder http://orcid.org/0000-0002-3472-1813.

References

Agostini, L., Touber, E. & Leschziner, M. A. 2014 Spanwise oscillatory wall motion in channel flow: drag-reduction mechanisms inferred from DNS-predicted phase-wise property variations at. *J. Fluid Mech.* **743**, 606–635.

Allen, J. 1977 Experimental study of error sources in skin-friction balance measurements. *J Fluid Engng.* **99**, 197–204.

Antonia, R., Kim, J. & Browne, L. 1991 Some characteristics of small-scale turbulence in a turbulent duct flow. *J. Fluid Mech.* **233**, 369–388.

Antonia, R. A., Zhu, Y. & Sokolov, M. 1995 Effect of concentrated wall suction on a turbulent boundary layer. *Phys. Fluids* **7**, 2465–2474.

Baars, W. J., Squire, D. T., Talluru, K. M., Abbassi, M. R., Hutchins, N. & Marusic, I. 2016 Wall-drag measurements of smooth- and rough-wall turbulent boundary layers using a floating element. *Exp. Fluids* **57**, 1–16.

Bai, H. L., Zhou, Y., Zhang, W. G., Xu, S. J., Wang, Y. & Antonia, R. A. 2014 Active control of a turbulent boundary layer based on local surface perturbation. *J. Fluid Mech.* **750**, 316–354.

BARON, A. & QUADRIO, M. 1996 Turbulent drag reduction by spanwise wall oscillations. *Appl. Sci. Res.* **55**, 311–326.

BENEDICT, L. H. & GOULD, R. D. 1996 Towards better uncertainty estimates for turbulence statistics. *Exp. Fluids* **22**, 129–136.

BERNARD, P. S., THOMAS, J. M. & HANDLER, R. A. 1993 Vortex dynamics and the production of Reynolds stress. *J. Fluid Mech.* **253**, 385–419.

BLACKWELDER, R. & KAPLAN, R. 1976 On the wall structure of the turbulent boundary layer. *J. Fluid Mech.* **76**, 89–112.

CANTON, J., ÖRLÜ, R., CHIN, C., HUTCHINS, N., MONTY, J. & SCHLATTER, P. 2016*a* On large-scale friction control in turbulent wall flow in low Reynolds number channels. *Flow Turbul. Combust.* **97**, 811–827.

CANTON, J., ÖRLÜ, R., CHIN, C. & SCHLATTER, P. 2016*b* Reynolds number dependence of large-scale friction control in turbulent channel flow. *Phy. Rev. Fluids* **1**, 081501.

CARLSON, H. A. & LUMLEY, J. L. 1996 Active control in the turbulent wall layer of a minimal flow unit. *J. Fluid Mech.* **329**, 341–371.

CHOI, K.-S. 2002 Near-wall structure of turbulent boundary layer with spanwise-wall oscillation. *Phys. Fluids* **14**, 2530.

CHOI, K.-S., DEBISSCHOP, J.-R. & CLAYTON, B. R. 1998 Turbulent boundary-layer control by means of spanwise-wall oscillation. *AIAA J.* **36**, 1157–1163.

CHOI, K. S., JUKES, T. & WHALLEY, R. 2011 Turbulent boundary-layer control with plasma actuators. *Phil. Trans. R. Soc. A* **369**, 1443–1458.

CHOI, H., MOIN, P. & KIM, J. 1993 Direct numerical simulation of turbulent flow over riblets. *J. Fluid Mech.* **255**, 503–539.

CHOI, K. S., YANG, X., CLAYTON, B. R., GLOVER, E. J., ATLAR, M., SEMENOV, B. N. & KULIK, V. M. 1997 Turbulent drag reduction using compliant surfaces. *Proc. R. Soc. A* **453**, 2229–2240.

CORKE, T. C., ENLOE, C. L. & WILKINSON, S. P. 2010 Dielectric barrier discharge plasma actuators for flow control. *Annu. Rev. Fluid Mech.* **42**, 505–529.

CORKE, T. C. & THOMAS, F. O. 2018 Active and passive turbulent boundary drag reduction. *AIAA J.* **56**, 3835–3847.

DANIELLO, R. J., WATERHOUSE, N. E. & ROTHSTEIN, J. P. 2009 Drag reduction in turbulent flows over superhydrophobic surfaces. *Phys. Fluids* **21**, 085103.

DE GRAAFF, D. B. & EATON, J. K. 2000 Reynolds number scaling of the flat-plate turbulent boundary layer. *J. Fluid Mech.* **422**, 319–346.

DU, Y., SYMEONIDIS, V. & KARNIADAKIS, G. E. 2002 Drag reduction in wall-bounded turbulence via a transverse travelling wave. *J. Fluid Mech.* **457**, 1–34.

ENDO, T., KASAGI, N. & SUZUKI, Y. 2000 Feedback control of wall turbulence with wall deformation. *Intl J. Heat Fluid Flow* **21**, 568–575.

ERSOY, S. & WALKER, J. D. A. 1985 Viscous flow induced by counter-rotating vortices. *Phys. Fluids* **28**, 2687–2698.

FUKAGATA, K., KERN, S., CHATELAIN, P., KOUMOUTSAKOS, P. & KASAGI, N. 2008 Evolutionary optimization of an anisotropic compliant surface for turbulent friction drag reduction. *J. Turbul.* **9**, 1–17.

HAKKINEN, R. 2004 Reflections on fifty years of skin friction measurement. In *24th AIAA Aerodynamic Measurement Technology and Ground Testing Conference*, pp. 1–13. AIAA.

HAMILTON, J. M., KIM, J. & WALEFFE, F. 1995 Regeneration mechanisms of near-wall turbulence structures. *J. Fluid Mech.* **287**, 317–348.

HUTCHINS, N. & CHOI, K.-S. 2002 Accurate measurements of local skin-friction coefficient using hot-wire enemometry. *Prog. Aerosp. Sci.* **38**, 421–446.

HURST, E., YANG, Q. & CHUNG, Y. M. 2014 The effect of Reynolds number on turbulent drag reduction by streamwise travelling waves. *J. Fluid Mech.* **759**, 28–55.

HUSSAIN, F. 1986 Coherent structures and turbulence. *J. Fluid Mech.* **173**, 303–356.

HUSSAIN, F. & DURAISAMY, K. 2011 Mechanics of viscous vortex reconnection. *Phys. Fluids* **23**, 021701.

IUSO, G., ONORATO, M., SPAZZINI, P. G. & DI CICCA, G. M. 2002 Wall turbulence manipulation by large-scale streamwise vortices. *J. Fluid Mech.* **473**, 23–58.

JEONG, J., HUSSAIN, F., SCHOPPA, W. & KIM, J. 1997 Coherent structures near the wall in a turbulent channel flow. *J. Fluid Mech.* **332**, 185–214.

JIMENEZ, J. & PINELLI, A. 1999 The autonomous cycle of near-wall turbulence. *J. Fluid Mech.* **389**, 335–359.

JUKES, T. N. & CHOI, K.-S. 2012 Dielectric-barrier-discharge vortex generators: characterisation and optimisation for flow separation control. *Exp. Fluids* **52**, 329–345.

JUKES, T. N. & CHOI, K.-S. 2013 On the formation of streamwise vortices by plasma vortex generators. *J. Fluid Mech.* **733**, 370–393.

JUKES, T. N., CHOI, K.-S., JOHNSON, G. A. & SCOTT, S. J. 2006 Characterization of surface plasma-induced wall flows through velocity and temperature measurements. *AIAA J.* **44**, 764–771.
KANG, S. & CHOI, H. 2000 Active wall motions for skin-friction drag reduction. *Phys. Fluids* **12**, 3301–3304.
KARNIADAKIS, G. E. & CHOI, K.-S. 2003 Mechanisms on transverse motions in turbulent wall flows. *Annu. Rev. Fluid Mech.* **35**, 45–62.
KIM, J. 1983 On the structure of wall-bounded turbulent flows. *Phys. Fluids* **26**, 2088–2097.
KIM, J. 2011 Physics and control of wall turbulence for drag reduction. *Phil. Trans. R. Soc. A* **369**, 1396-411.
KIM, J., KIM, K. & SUNG, H. J. 2003 Wall pressure fluctuations in a turbulent boundary layer after blowing or suction. *AIAA J.* **41**, 1697–1704.
KLINE, S. J., REYNOLDS, W., SCHRAUB, F. & RUNSTADLER, P. 1967 The structure of turbulent boundary layers. *J. Fluid Mech.* **30**, 741–773.
KRAVCHENKO, A. G., CHOI, H. & MOIN, P. 1993 On the relation of near-wall streamwise vortices to wall skin friction in turbulent boundary layers. *Phys. Fluids* **5**, 3307–3309.
KROGSTAD, P-Å & EFROS, V. 2010 Rough wall skin friction measurements using a high resolution surface balance. *Intl J. Heat Fluid Flow* **31**, 429–433.
LI, W., JESSEN, W., ROGGENKAMP, D., KLAAS, M., SILEX, W., SCHIEK, M. & SCHRÖDER, W. 2015 Turbulent drag reduction by spanwise traveling ribbed surface waves. *Eur. J. Mech. B/Fluids)* **53**, 101–112.
LI, W., ROGGENKAMP, D., JESSEN, W., KLAAS, M. & SCHRÖDER, W. 2017 Reynolds number effects on the fluctuating velocity distribution in wall-bounded shear layers. *Meas. Sci. Technol.* **28**, 015302.
LÖGDBERG, O., FRANSSON, J. H. M. & ALFREDSSON, P. H. 2009 Streamwise evolution of longitudinal vortices in a turbulent boundary layer. *J. Fluid Mech.* **623**, 27–58.
MAHFOZE, O. & LAIZET, S. 2017 Skin-friction drag reduction in a channel flow with streamwise-aligned plasma actuators. *Intl J. Heat Fluid Flow* **66**, 83–94.
MIZUMOTO, H., HOSOKAWA, S., SUZUKI, T. & TOMIYAMA, A. 2012 Evaluation of turbulence kinetic energy budget in turbulent flows by using a photobleaching molecular tagging velocimetry. *AIP Conf. Proc.* **1428**, 295–302.
MOREAU, E. 2007 Airflow control by non-thermal plasma actuators. *J. Phys. D Appl. Phys.* **40**, 605–636.
NAGIB, H. M., CHAUHAN, K. A. & MONKEWITZ, P. A. 2007 Approach to an asymptotic state for zero pressure gradient turbulent boundary layers. *Phil. Trans. R. Soc. A* **365**, 755–770.
ORLANDI, P. & JIMÉNEZ, J. 1994 On the generation of turbulent wall friction. *Phys. Fluids* **6**, 634–641.
PARK, J. & CHOI, H. 1999 Effects of uniform blowing or suction from a spanwise slot on a turbulent boundary layer flow. *Phys. Fluids* **11**, 3095–3105.
PAULEY, W. R. & EATON, J. K. 1988 Experimental study of the development of longitudinal vortex pairs embedded in a turbulent boundary layer. *AIAA J.* **26**, 816–823.
POPE, S. B. 2001 *Turbulent Flows*. Cambridge University Press.
QIAO, Z. X., WU, Z. & ZHOU, Y. 2018 Turbulent boundary layer manipulation under a proportional-derivative closed-loop scheme. *Phys. Fluids* **30**, 115101.
QIAO, Z. X., XU, S. J. & ZHOU, Y. 2019 On the measurement of wall-normal velocity derivative in a turbulent boundary layer. *Flow Turbul. Combust* **103**, 369–387.
QIAO, Z. X., ZHOU, Y. & WU, Z. 2017 Turbulent boundary layer under the control of different schemes. *Proc. R. Soc. A* **473**, 20170038.
QUADRIO, M., RICCO, P. & VIOTTI, C. 2009 Streamwise-travelling waves of spanwise wall velocity for turbulent drag reduction. *J. Fluid Mech.* **627**, 161–178.
RASTEGARI, A. & AKHAVAN, R. 2015 On the mechanism of turbulent drag reduction with super-hydrophobic surfaces. *J. Fluid Mech.* **773**, R4.
RATHNASINGHAM, R. & BREUER, K. S. 2003 Active control of turbulent boundary layers. *J. Fluid Mech.* **495**, 209–233.
RICCO, P. & WU, S. 2004 On the effects of lateral wall oscillations on a turbulent boundary layer. *Exp. Therm. Fluid Sci.* **29**, 41–52.
SCHLATTER, P., ÖRLÜ, R., LI, Q., BRETHOUWER, G., FRANSSON, J. H. M., JOHANSSON, A. V., ALFREDSSON, P. H. & HENNINGSON, D. S. 2009 Turbulent boundary layers up to $Re_\theta = 2500$ studied through simulation and experiment. *Phys. Fluids* **21**, 051702.
SCHOPPA, W. & HUSSAIN, F. 1998 A large-scale control strategy for drag reduction in turbulent boundary layers. *Phys. Fluids* **10**, 1049–1051.
SCHOPPA, W. & HUSSAIN, F. 2002 Coherent structure generation in near-wall turbulence. *J. Fluid Mech.* **453**, 57–108.
SCIACCHITANO, A. & WIENEKE, B. 2016 PIV uncertainty propagation. *Meas. Sci. Technol.* **27**, 084006.
SPALART, P. R. 1988 Direct simulation of a turbulent boundary layer up to $Re_\theta = 1410$. *J. Fluid Mech.* **187**, 61–98.

TARDU, S. F. 2001 Active control of near-wall turbulence by local oscillating blowing. *J. Fluid Mech.* **439**, 217–253.

THOMAS, F. O., CORKE, T. C., DUONG, A., MIDYA, S. & YATES, K. 2019 Turbulent drag reduction using pulsed-DC plasma actuation. *J. Phys. D: Appl. Phys.* **52**, 434001.

THOMAS, F. O., CORKE, T. C., IQBAL, M., KOZLOV, A. & SCHATZMAN, D. 2009 Optimization of dielectric barrier discharge plasma actuators for active aerodynamic flow control. *AIAA J.* **47**, 2169–2178.

WALLACE, J. M. 2016 Quadrant analysis in turbulence research: history and evolution. *Annu. Rev. Fluid Mech.* **48**, 131–158.

WALSH, M. J. 1983 Riblets as a viscous drag reduction technique. *AIAA J.* **21**, 485–486.

WANG, L., WONG, C. W., LU, Z., WU, Z. & ZHOU, Y. 2017 Novel sawtooth dielectric barrier discharge plasma actuator for flow separation control. *AIAA J.* **55**, 1405–1416.

WHALLEY, R. D. & CHOI, K.-S. 2014 Turbulent boundary-layer control with plasma spanwise travelling waves. *Exp. Fluids* **55**, 1796.

WICKS, M., THOMAS, F. O., CORKE, T. C., PATEL, M. & CAIN, A. B. 2015 Mechanism of vorticity generation in plasma streamwise vortex generators. *AIAA J.* **53**, 3404–3413.

WONG, C. W., WANG, L., MA, W. & ZHOU, Y. 2020 New sawtooth plasma actuator configuration and mechanism behind improved control performance. *AIAA J.* **58**, 1881–1886.

YAO, J., CHEN, X. & HUSSAIN, F. 2018 Drag control in wall-bounded turbulent flows via spanwise opposed wall-jet forcing. *J. Fluid Mech.* **852**, 678–709.

YAO, J., CHEN, X., THOMAS, F. & HUSSAIN, F. 2017 Large-scale control strategy for drag reduction in turbulent channel flows. *Phy. Rev. Fluids* **2**, 062601.

YAO, J. & HUSSAIN, F. 2020 A physical model of turbulence cascade via vortex reconnection sequence and avalanche. *J. Fluid Mech.* **883**, A51.